

MASTER

Liquid circulation in a micro-structured bubble column

An experimental and numerical study of liquid circulation in a micro- structured bubble column

Kuiper, Max A.

Award date:
2016

[Link to publication](#)

Disclaimer

This document contains a student thesis (bachelor's or master's), as authored by a student at Eindhoven University of Technology. Student theses are made available in the TU/e repository upon obtaining the required degree. The grade received is not published on the document as presented in the repository. The required complexity or quality of research of student theses may vary by program, and the required minimum study period may vary in duration.

General rights

Copyright and moral rights for the publications made accessible in the public portal are retained by the authors and/or other copyright owners and it is a condition of accessing publications that users recognise and abide by the legal requirements associated with these rights.

- Users may download and print one copy of any publication from the public portal for the purpose of private study or research.
- You may not further distribute the material or use it for any profit-making activity or commercial gain

Master Thesis

Liquid circulation in a micro-structured bubble column

An experimental and numerical study of liquid circulation in a micro-structured bubble column

M.A. Kuiper

Eindhoven, 17-5-2016



Graduation committee

Prof.dr.ir. J.A.M. Kuipers

Prof.dr.ir. N.G. Deen

Prof.dr.ir. J. Meuldijk

MSc. K. Thiruvalluvan Sujatha

Table of Contents

Abstract.....	1
List of symbols	2
1 Introduction	5
1.1 Bubble column	5
1.2 Flow regimes	6
1.3 Liquid circulation.....	7
1.4 Micro-structured bubble column.....	8
1.5 Experimental techniques.....	10
1.6 Scope and objective of research.....	10
1.7 Outline of intermediate report	10
2 Experimental setup and measurement techniques.....	11
2.1 Experimental setup	11
2.2 Digital image analysis	12
2.3 Particle image velocimetry.....	15
2.4 Gas holdup.....	16
2.5 Chemisorption experiments.....	17
2.5.1 Reaction kinetics	17
2.5.2 Physical absorption	19
2.5.3 Chemical enhancement.....	19
2.5.4 Experiments procedure.....	20
2.6 Tracer experiments	20
3 Experimental results.....	23
3.1 Visual observation.....	23
3.1.1 Results.....	25
3.1.2 Chosen parameter space for hydrodynamic study	26
3.2 Hydrodynamic study.....	26
3.2.1 Influence of liquid velocity	27
3.2.2 Influence of structured packings.....	31
3.3 Results tracer experiments.....	34

4	Modelling micro-structured bubble column	37
4.1	Model description.....	37
4.2	Balances	38
4.2.1	Liquid phase	38
4.2.2	Gas phase	39
4.3	Solution strategy.....	40
4.4	Bubble cutting implementation.....	41
4.5	Result sample.....	41
4.6	Validation parameters.....	42
5	Validation of CSTRs in series model.....	44
5.1	Case 1: Homogeneous regime	44
5.2	Case 2: Transition regime	46
6	Conclusions.....	49
7	Recommendations.....	51
	Acknowledgements	52
	Bibliography	53
	Appendix I: Visual observation results.....	55
	Appendix II: Bubble size and VPD at low superficial gas velocities.....	57
	Appendix III: Sherwood correlations	58
	Appendix IV: Discretization and boundary conditions.....	59
	Appendix V: Sensitivity analysis CSTRs in series model	61

Abstract

Bubble columns are used in industry as gas-liquid contactors and have a wide variety of applications. Most bubble columns are utilized with internal structures. These structures are inserted to control flow structures, increase gas holdup, heat transfer or to decrease back mixing and bubble size in the column. Wire-meshes are used as internal structures in this investigation to decrease bubble size by the cutting of bubbles. Bubble cutting increases the specific surface area of bubbles and enhances the mass transfer rates in the column. The wire-meshes are cheap, occupy less volume and have a lower pressure drop compared to other structures. These meshes could also be coated with catalyst to operate as a three-phase reactor.

In this project, co-current liquid circulation is investigated experimentally and numerically by using wire-meshes in a pseudo-2D bubble column. The influence of liquid circulation on hydrodynamics is experimentally investigated in an air-water system. Different internal structures are compared by varying superficial gas and liquid velocities. The numerical investigation consist of a continuous stirred tank reactors (CSTRs) in series model to describe the micro-structured bubble column for a reactive $\text{CO}_2\text{-NaOH}$ system.

In the hydrodynamic study two wire-meshes (mesh openings of 2.7 and 3.6 mm) are compared to a Sulzer packing with different superficial gas and liquid velocities. Bubble size in the bubble column is measured by using the digital image analysis (DIA) technique. Bubble velocities in the column are measured by the particle image velocimetry (PIV) technique. Bubble size is found to increase with increasing liquid velocity. Additionally, the liquid circulation did not enhance the bubble cutting performance. Best cutting performance is obtained for a wire-mesh with openings of 3.6 mm (highest difference in Sauter mean diameter Δd_{32}). Interestingly, the Sulzer packing had the lowest cutting performance of all studied inserts. This might be caused by the lower bubble velocities near the mesh that reduces the force for the cutting of bubbles. Furthermore, bubble velocities are most significantly increased from a superficial liquid velocity of 0 to 7 mm/s. Increasing liquid velocity to 14 and 28 mm/s did not result in a significantly higher bubble velocity. This result coincided with the results from the gas holdup which decreases most significantly from 0 to 7 mm/s.

The micro-structured bubble column is modelled using a CSTRs in series model and validated by two cases. Case 1 is performed with a low superficial gas velocity and intermediate superficial liquid velocity in the homogeneous regime. The experiments matches the model well and showed that kinetics, gas velocity and liquid compartment linkage was properly implemented. At the end of the reaction, a slight deviation was found which might be caused by the coalescence of bubbles. Case 2 is performed in the transition regime, with a higher superficial gas velocity and lower superficial liquid velocity. In this case the mismatch of the model compared to experiments was more significant. This was caused by the higher coalescence rate of bubbles which was observed from the recorded images.

List of symbols

A	Area	$[\text{m}^2]$
\bar{N}	Average number	$[-]$
\bar{V}	Average volume	$[\text{m}^3]$
d_{bin}	Bin width	$[\text{m}]$
$[X]$	Concentration of component X	$[\text{mol}_X \cdot \text{m}_l^{-3}]$
ρ	Density	$[\text{kg} \cdot \text{m}^{-3}]$
d	Diameter	$[\text{m}]$
D	Diffusivity coefficient	$[\text{m}_2 \cdot \text{s}^{-1}]$
Δx	Displacement	$[\text{m}]$
C_d	Drag coefficient	$[-]$
E	Enhancement factor	$[-]$
EO	Eötvös Number	$[-]$
N	Equivalent bubble diameter	$[\text{pixels}]$
ΔN	Fractional error	$[-]$
z	Gas compartment number	$[-]$
Δz	Height of one CSTR	$[\text{m}]$
h	Height of the bubble column	$[\text{m}]$
H	Henry coefficient	$[\text{m}_g^3 \cdot \text{m}_l^{-3}]$
ε	Holdup	$[\text{m}_l^3 \cdot \text{m}_r^{-3}]$
I	Image matrix	$[-]$
L_1	Length of the cylindrical part of vessel 1	$[\text{m}]$
k_l	Mass transfer coefficient	$[\text{m} \cdot \text{s}^{-1}]$
M	Molar mass	$[\text{kg} \cdot \text{m}^{-3}]$
N_{CSTR}	Number of CSTR's to simulate gas phase	$[-]$
S	Perimeter	$[\text{m}]$
PDF	Probability density function	$[\text{m}^{-1}]$
r	Reaction rate	$[\text{mol} \cdot \text{m}^{-3} \cdot \text{s}^{-1}]$
k	Reaction rate constant	$[1/\text{s}]$ or $[\text{m}^3 \cdot \text{mol}^{-1} \cdot \text{s}^{-1}]$ (depends on order of reaction)
Re	Reynolds number	$[-]$
Ro	Roundness factor	$[-]$
$a = \frac{A}{V}$	Specific surface area	$[\text{m}^{-1}]$
t	Time	$[\text{s}]$

Δt	Time step	[s]
u	Velocity	[m · s ⁻¹]
V	Volume	[m ³]
VPD	Volumetric probability density	[m ⁻¹]

Superscripts

$BC1$	Bubble column 1, corresponding to Figure 4.1.
$BC2$	Bubble column 2, corresponding to Figure 4.1.
X	Compartment BC1, BC2 or V1 corresponding to Figure 4.1 and used in Equation 4.1 to 4.4.
$V1$	Side vessel 1, corresponding to Figure 4.1.
sup	Superficial

Subscripts

$1,2$	Backward reaction corresponding to Equation (2.2)
$2,2$	Backward reaction corresponding to Equation (2.3)
b	Bubble
CO_2	Carbon dioxide
$1,1$	Forward reaction corresponding to Equation (2.2)
$2,1$	Forward reaction corresponding to Equation (2.3)
g	Gas
l	Liquid
r	Reactor

Abbreviations

BC1	Bubble column 1, corresponding to Figure 4.1.
BC2	Bubble column 2, corresponding to Figure 4.1.
CSTR	Continuous stirred tank reactor
DIA	Digital image analysis
MT	Mass transfer
MSBC	Micro-structured bubble column
PIV	Particle image velocimetry

PFR Plug flow reactor
PDEng Professional doctorate in Engineering, post-MSc program
V1 Side vessel 1, corresponding to Figure 4.1.

1 Introduction

1.1 Bubble column

Bubble columns are widely used in industry as gas-liquid contactors and have many advantages. Bubble columns have excellent mass and heat transfer characteristics. Most importantly, bubble columns require low maintenance and operation cost, due to the lack of mechanical moving parts. Gas is usually fed to the bottom of the column, while the liquid flow can be operated co-currently or counter-currently with respect to the gas flow. These bubble columns mostly involve fast chemical reactions in the liquid phase and are therefore mostly limited by mass transfer.

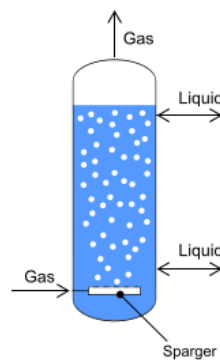


Figure 1.1: Schematic representation of a bubble column for co- and counter-current configuration.

The coupling of relevant phenomena inside the column is illustrated in Figure 1.2. The chemical reaction rate depends on the local availability of the absorbed species, which dependent on the mass transfer. The mass transfer depends on the specific surface area, mass transfer coefficient and on the reaction rate via the Enhancement factor (E). The bubble diameter is an important parameter as it influences the hydrodynamics and mass transfer. Smaller bubble size implies a relatively larger interfacial area and, therefore, a larger mass transfer rate. Small bubble size can be achieved by using a structured packing.

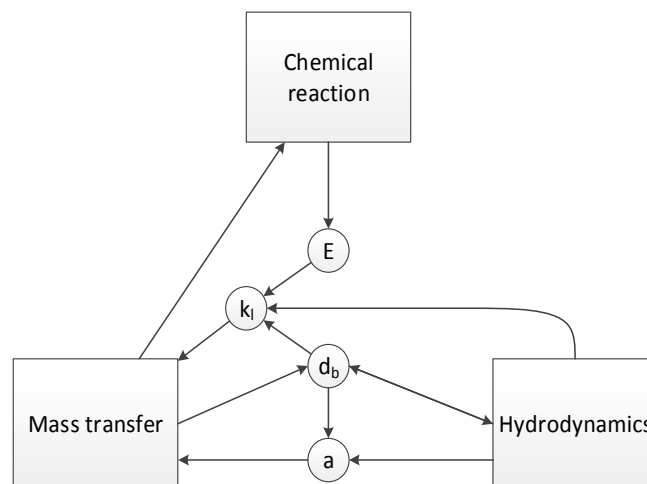


Figure 1.2: Inter-dependency diagram of chemical reaction, mass transfer and hydrodynamics in a bubble column [1].

1.2 Flow regimes

The regimes in a bubble column can be classified into three regimes, based on the superficial gas velocity and the reactor diameter. The homogeneous regime is the regime where small bubbles with a narrow distribution in size exist. This occurs at low superficial gas velocities from 0 to 0.05 m/s. Higher gas flow rates result in more turbulence and this is called the heterogeneous or churn turbulent regime. In this regime, a wide range of bubble sizes are present. This regime is predominantly encountered in industry. The third regime is slug flow, which occurs when small columns are operated at high superficial gas velocity. The wall stabilizes the bubbles and slugs are formed. This regime is not desirable if high interaction between gas and liquid are required. Figure 1.3 depicts a schematic representation of the flow regimes.

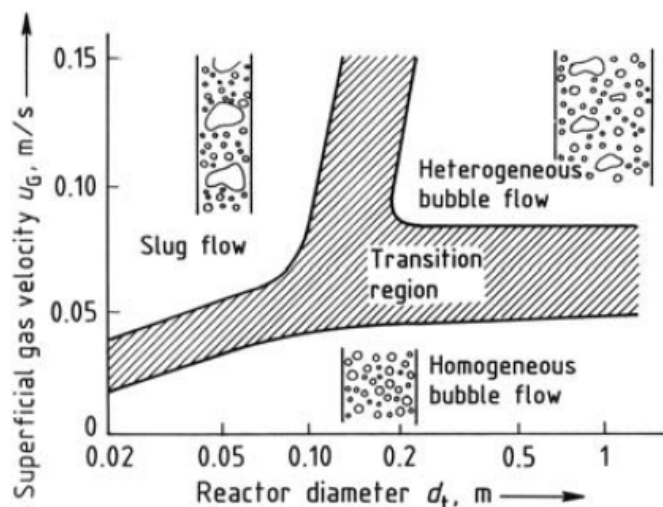


Figure 1.3: Flow regimes in a bubble column [2].

In these regimes different bubble sizes are seen, which have a different bubble rise velocities in the bubble column. Additionally, the gas holdup is dependent on these bubble rise velocity, since small rise velocities result in longer residence time and higher holdup. Therefore, dependency of bubble rise velocity on the bubble size is displayed in Figure 1.4 for an air-water system. It is observed that the bubble rise velocity increases for bubble size from 0 to 2.8 mm, but after 2.8 mm the drag force becomes more significant and the bubble rise velocity remains around 0.25 m/s.

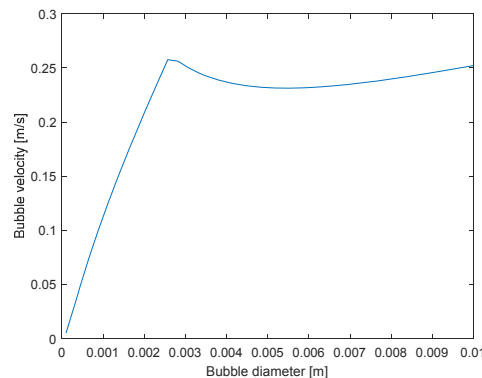


Figure 1.4: Bubble rise velocity versus bubble diameter in an air-water system

1.3 Liquid circulation

Liquid circulation in bubble columns has been investigated, but mostly without internal structures. A downside of liquid circulation is the decrease of gas holdup in co-current operation (Bin [3], Pjontek [4] and Jin [5]). On the other side counter-current operation increases gas holdup. Figure 1.5 indicates the influence of liquid circulation on gas holdup.

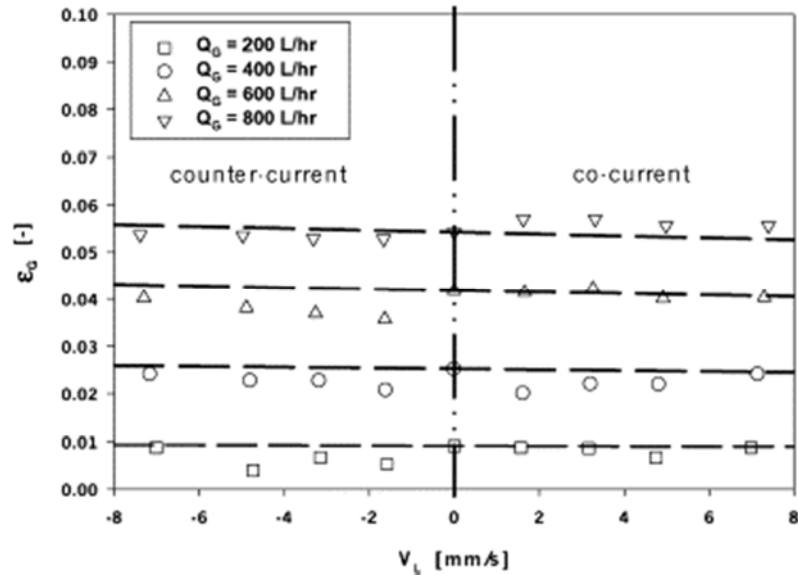


Figure 1.5: Gas holdup versus superficial liquid velocity for co-current or counter-current operation [3].

Meeusen [6] showed the potential of liquid circulation on bubble cutting with the use of a wire-mesh. Liquid circulation reduces the formation of a gas pocket or gas cushion (Figure 1.6). This phenomenon is observed when wire-meshes with openings smaller than 3.3 mm are used. Contributing to this, Höller [7] and Rabha [8] showed that co-current liquid circulation increases the pressure drop over a structured packing. This extra force might improve the cutting behaviour of bubbles.

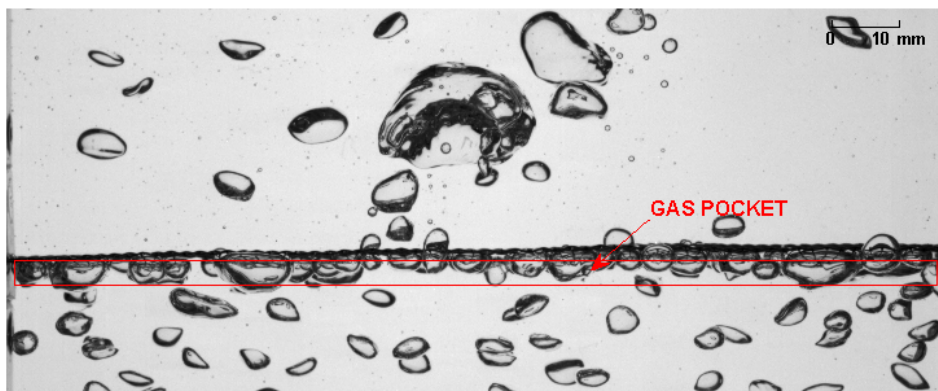


Figure 1.6: Gas pocket observation under the wire-mesh in a pseudo-2D bubble column [2].

1.4 Micro-structured bubble column

Various modifications in bubble columns have been proposed, often equipped with sieve trays, structured packings or vertical shafts. Figure 1.7 shows some modified bubble columns that are used in industry [3]. Most industrial bubble column reactors are utilized with internal structures. These structures are used to control flow structures, increase gas holdup, heat transfer or to decrease back mixing and bubble size in the column.

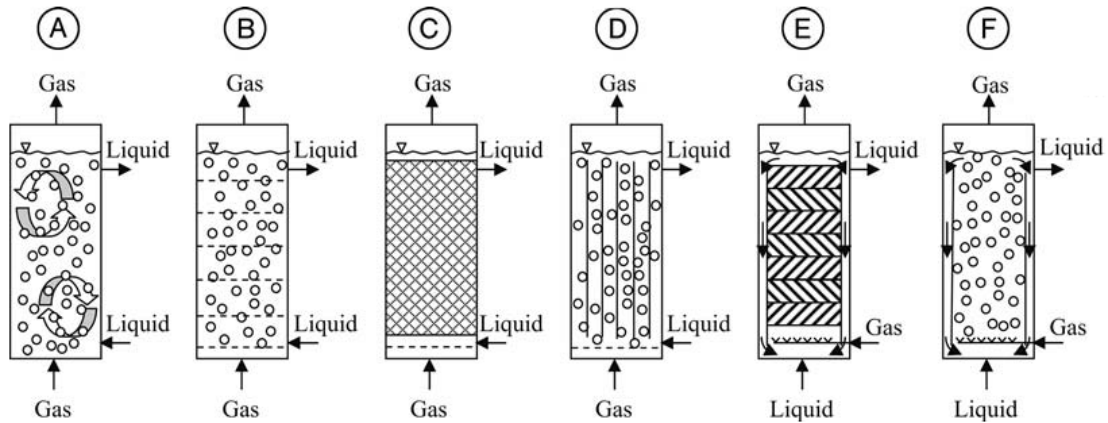


Figure 1.7: Different types of bubble column reactors. A: Simple bubble column, B: Cascade bubble column with sieve trays, C: Packed bubble column, D: Multishaft bubble column, E: Bubble column with static mixers, F: Airlift loop reactor (Deen [9]).

In this study, a micro-structured bubble column (MSBC) is investigated that uses wire-meshes to reduce bubble size by cutting the bubbles. Bubble cutting reduces the bubble size, which increases the specific surface area resulting in the desirable increase of mass transfer rates. Wire-meshes are available in different shapes and different opening sizes. A wire-mesh occupies less volume, reduces back mixing and is much cheaper than a structured packing. Also the pressure drop over a wire-mesh is relatively lower than other structured packings, because less drag is exerted on the fluid due to the open structure. Another advantage is that if multiple meshes are inserted in series and coated with a catalyst, the system can be operated as a three-phase reactor.

A considerable amount of literature has been published on structured meshes. Höller [10] studied fibrous woven materials as structured catalyst and reported that pressure drop and gas holdup depend on the distance between fibre threads. Chen and Yang [11] have studied characteristics of multi-stage stainless steel wire-mesh screen plates and found that diameter effects of the column are minimal, which simplifies the scale-up process.

Thiruvalluvan Sujatha [2] studied different wire-meshes in an air-water system in a pseudo-2D bubble column for different flow configurations and discovered that bubbles are slowed down by the mesh with small openings (less than 3.3 mm). Moreover, Thiruvalluvan Sujatha showed that bubbles tend to re-coalesce after passing through the mesh as shown in Figure 1.8.

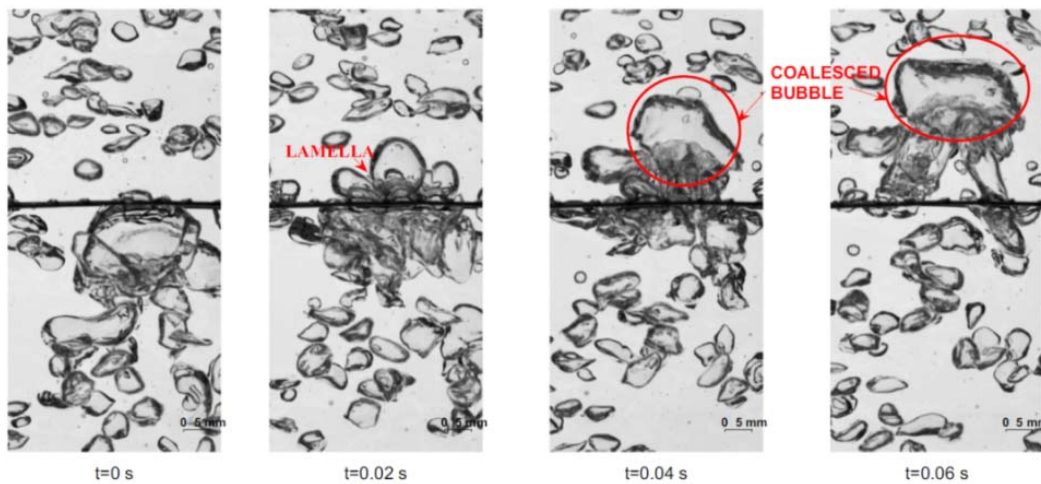


Figure 1.8: Re-coalescence of bubbles after the mesh. Configuration 5.6 mm and $u_g = 30$ mm/s [2].

Bubble sizes are strongly influenced by the surface tension. Asgharpour [12] investigated the influence of contamination on oxygen mass transfer and showed that hydrocarbon contamination lowers the surface tension of the liquid. Kamath [13] partly expanded Thiruvalluvan Sujatha's investigation by looking at the influence of surface tension on bubble cutting. This investigation was performed with nitrogen gas and a liquid with a lower surface tension: dodecane. Cutting was observed at lower gas velocities and cutting occurred at smaller mesh openings than in the air-water system. During this investigation the phenomena of decreasing bubble size due to contamination was also observed. Figure 1.9 depicts the difference between a contaminated and a clean column.

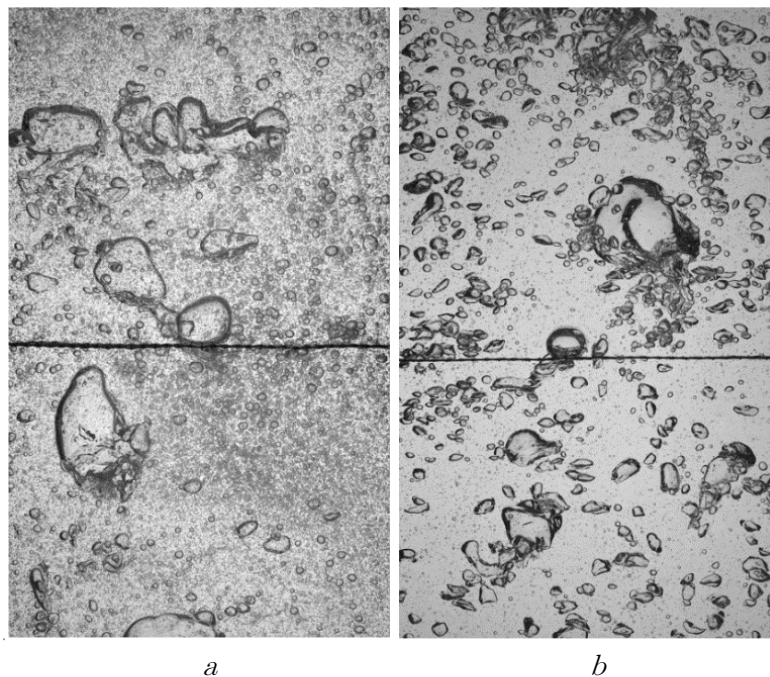


Figure 1.9: The difference in bubble size between a contaminated column (a) and clean column (b). Configuration: wire-mesh openings of 3.6 mm, $u_g = 30$ mm/s, $u_l = 0$ mm/s.

1.5 Experimental techniques

To measure bubble dynamics and reaction progress in the column different experimental techniques are used. Two types of techniques are available: intrusive and non-intrusive. Intrusive methods interfere with the hydrodynamics, like conductivity probes [7], pH meter [13] or capillary suction probes [11]. On the other side non-intrusive methods do not affect the flow, like digital image analysis (DIA) [2], Electrical resistance tomography [5] or particle image velocimetry (PIV) [2]. For studying bubble dynamics, the use of a non-intrusive method is preferred to eliminate the influence of the measurement on the behaviour in the column. Therefore, DIA and PIV are used to study bubble dynamics and are discussed in Chapter 2.

1.6 Scope and objective of research

The cutting of bubbles with wire-meshes has extensively been investigated, to reduce bubble diameters and subsequently enhancing mass transfer. However, little is known about the influence of liquid circulation on bubble cutting and hydrodynamics of the system. The liquid flow impacts hydrodynamics and might exert an extra force on the bubbles which is expected to improve the cutting behaviour. Therefore, the focus of this study is on cutting behaviour of different internals with co-current gas-liquid flow.

The study is divided into two parts. First, a hydrodynamic investigation in a non-reactive air-water system is performed. Wire-meshes and an industrially used Sulzer packing are investigated for different gas and liquid velocities. This yields the influence of co-current liquid velocity on hydrodynamics and bubble cutting behaviour. The second part consist of a numerical investigation. The MSBC is modelled and validated for the chemisorption reaction of CO₂ and NaOH. This model includes the effect of liquid circulation inside the bubble column.

1.7 Outline of intermediate report

Chapter 2 explains different experimental techniques used in this research. Chapter 3 discusses the results of the experiments to see the influence of liquid velocity on hydrodynamics and bubble cutting. Chapter 4 describes the model description for a MSBC with liquid re-circulation. Validation of the model is discussed in Chapter 5. Finally the conclusion and recommendation are presented in Chapter 6 and 7 respectively.

2 Experimental setup and measurement techniques

2.1 Experimental setup

Experiments are carried out in a pseudo-2D bubble column with an overflow vessel. The column is made of transparent glass to enable visual observation by the camera. A schematic representation of the column is shown in Figure 2.1. Gas is distributed by three channels which are individually controlled by a volumetric flow controller. Each individual channel is distributed over 5 gas needles and led to the distributor plate in the bottom of the column. Liquid is recycled through a storage vessel and pumped back into the column at the bottom.

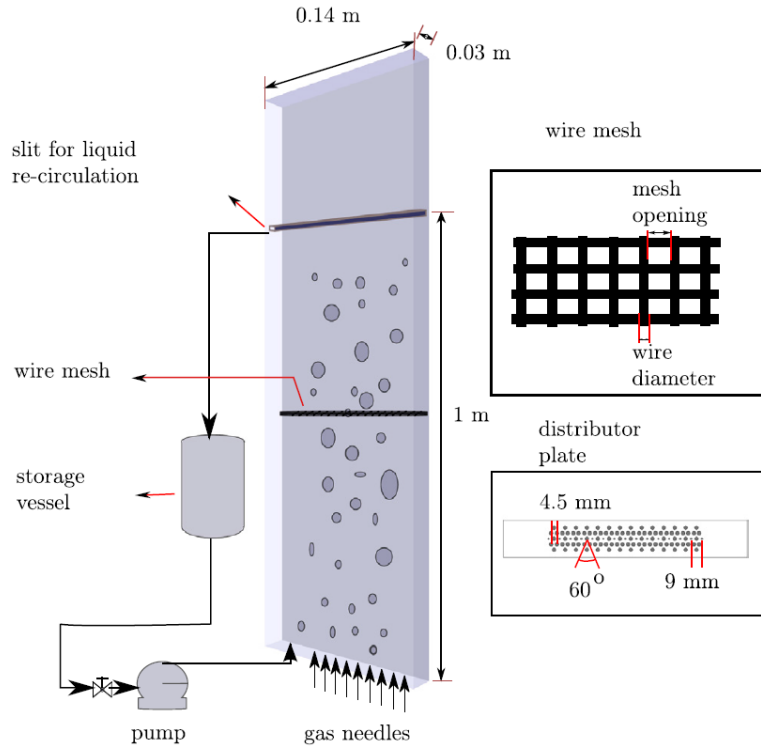


Figure 2.1: Schematic representation of the experimental setup: the micro-structured bubble column (MSBC). Additionally, a schematic representation of the wire-mesh properties and the distributor plate on the bottom of the column [2].

When the gas and liquid flow are set, the system is allowed to stabilize for 15 minutes. The camera is focussed on the middle section of the column where the wire-mesh is placed approximately 50 cm above the bottom. The camera observes a small section (± 22 cm) to maintain adequate spatial resolution to perform image analysis. Each experiment records 4000 images at 50 Hz. When the images are recorded, the flow-rates are modified and the procedure is repeated.

2.2 Digital image analysis

Bubble detection is performed by using an image algorithm. This algorithm consists of four main operations: (a) Image filtering, (b) separation of solitary from overlapping bubbles, (c) watershedding technique on overlapping bubbles and (d) combining the results of solitary with overlapping bubbles. This process is schematically represented in Figure 2.2 and the different operations are described here in more detail.

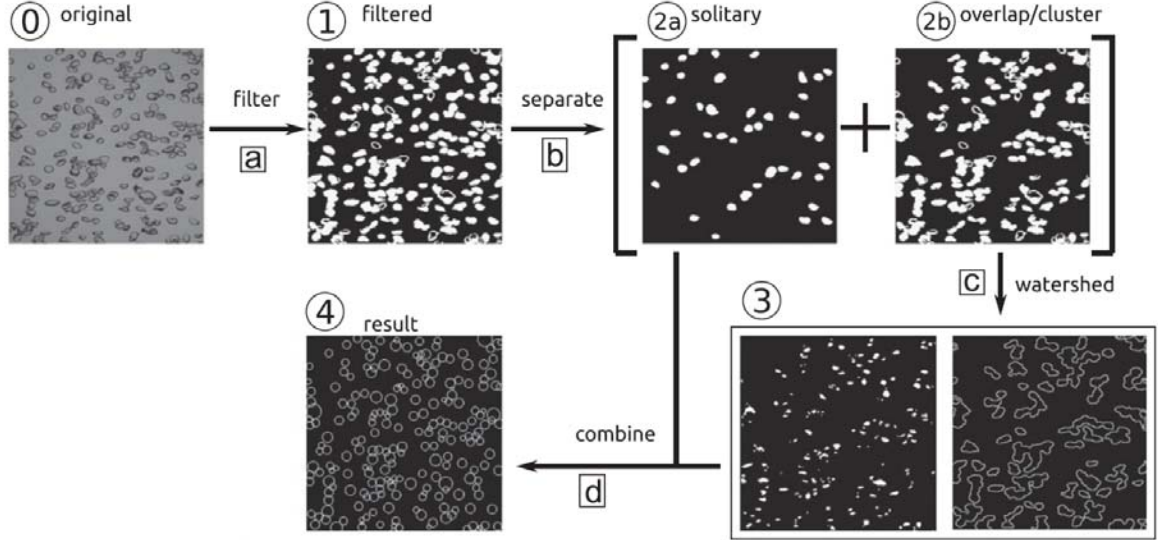


Figure 2.2: Schematic representation of image algorithm performed in digital image analysis [14].

Image filtering (a): In the first step, the images from the high speed camera are run through a number of filters, see Figure 2.3.

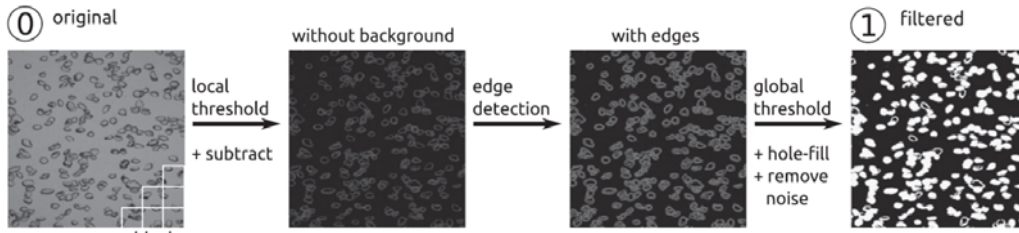


Figure 2.3: Image filtering process (a) in digital image analysis [14].

First local thresholding is performed to remove the inhomogeneous background. Local thresholding is carried out in equally defined block sizes of the image, where the background of these individual blocks is assumed to be homogenous. Each block is thresholded independently by using a filter function proposed by Otsu (1979):

$$I_{local\ threshold}(i, j) = \begin{cases} 0 & \text{if } I_0(i, j) \geq I_{otsu} \\ 1 & \text{if } I_0(i, j) \leq I_{otsu} \end{cases}$$

Where I_{Otsu} is the automatic threshold level. The local $I_{\text{local threshold}}$ is subtracted from the original image (I_0) to obtain the image without background.

$$I_{\text{background removed}} = I_0 - I_{\text{local threshold}}$$

After removing the background, edge detection is performed. This procedure highlights the edge using an edge detection algorithm proposed by Canny (1986). This enhances the distinction between bubbles and background:

$$I_{\text{edge}} = I_{\text{background removed}} - \text{edge}(I_{\text{background removed}})$$

In the third step of the filtering process, a binary image I_1 is obtained from I_{edge} by choosing an appropriate threshold value $I_{\text{histogram}}$:

$$I_1(i, j) = \begin{cases} 0 & \text{if } I_{\text{edge}}(i, j) \geq I_{\text{histogram}} \\ 1 & \text{if } I_{\text{edge}}(i, j) \leq I_{\text{histogram}} \end{cases}$$

After the binary image is made, bubbles smaller than the minimal area (A_{min}) are removed as noise. Finally the filtering process ends by filling the holes, this operation fills the inside of the bubbles with the same intensity as the walls.

Separate image (b): the filtered image (I_1) is separated into solitary and overlapping bubbles. This operation is performed by comparing the roundness of the objects, this is defined as:

$$Ro = \frac{S}{\sqrt{4\pi \cdot A}} \quad 2.1$$

Where S is the perimeter and A the area of the object. Note that spherical bubbles have a roundness of unity. In this analysis an object is defined as solitary if the roundness is smaller than 1.25, as suggested by Lau [14]. The resulting image with solitary bubbles (2a in Figure 2.2) is segmented by labelling the solitary bubble areas. While the overlapping bubbles (2b) are segmented in the next step (c) using the watershedding technique proposed by Meyer (1994).

Watershedding technique (c): To distinguish bubbles from overlapping bubbles, watershedding is used, which is illustrated in Figure 2.4. The original image contains 3 overlapping bubbles which are displayed in (Figure 2.4a). The background and solitary bubbles are removed from the original image, which is then inverted, resulting in (Figure 2.4b). After inverting the image, it is thresholded to acquire the bubble markers as local minima (Figure 2.4c). Adding local borders to the local minima image gives (Figure 2.4d). This image is then flooded from below by letting water rise through the minima forming three basins. The line where two flooding basins meet yields the watershed lines, which lead to three distinct bubbles, displayed in sub image (Figure 2.4e). The illustration of this watershed transformation in a two-dimensional plane is illustrated by Figure 2.5.

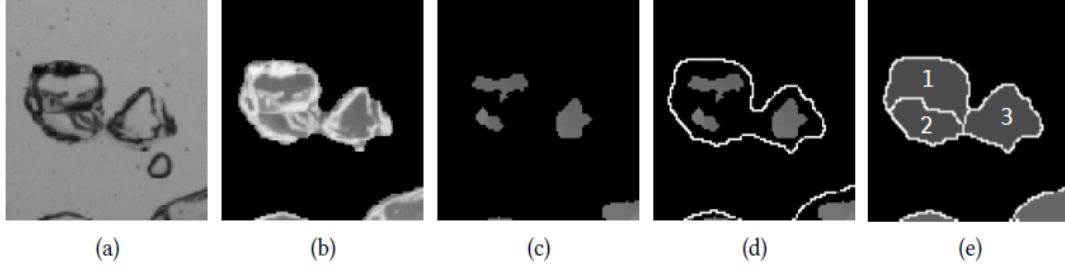


Figure 2.4: An example of the watershedding process: (a) part of the original image with a group of three overlapping bubbles, (b) inverted image with background and solitary bubbles masked out, (c) bubble markers as local minima are acquired by thresholding image, (d) adding local border to the local minima and (e) three distinct bubbles are found by the flooded image [14].

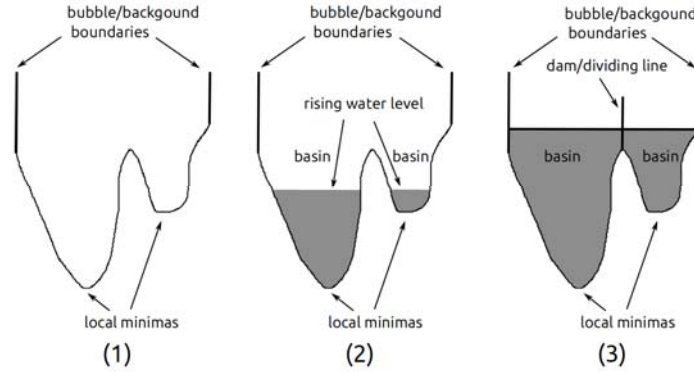


Figure 2.5: Illustration of the watershed transformation in a two-dimensional plane: (1) starting from the local minima of the bubbles, (2) the basins or bubble areas are flooded and (3) dams or watershed lines are formed dividing the bubbles from each other [15].

Combining the images (d): The last step combines the images of the solitary bubbles with the results found after watershedding ($I_{2a} + I_3$). This yields an overall image (I_4) where all bubbles are drawn as circles. The result of bubble size is based on dimensions in pixels, this is converted to metric values. From the detected area the equivalent diameter is calculated as shown in Equation 2.2.

$$d_e = \sqrt{\frac{4A}{\pi}} \quad 2.2$$

In the MATLAB® code developed by Lau [14], a maximum and minimum detectable bubble area are set. This is due to the fact that noise is detected as small bubbles, therefore, the minimum bubble area is set to 10 pixels. False bubble detection occurs and the maximum bubble area is set to 10000 pixels.

Validation digital image analysis script

The images taken from the camera are analysed with the digital image analysis algorithm using MATLAB® R2015a. The validation is done by looking at several images and the detection of the script, an example is given in Figure 2.6. The figure shows minor complications with the detection, as some bubbles have been identified incorrectly. Moreover, some bubbles are not

detected, because their borders are insufficiently dark. Detection could also fail when a lot of bubbles are present and overlap, this was observed in the MSBC from gas holdup of around 0.1 for no liquid circulation. In that case the algorithm has difficulty to distinguish between the background and the bubbles. Lau [14] discussed the limitations of the DIA technique in more detail.

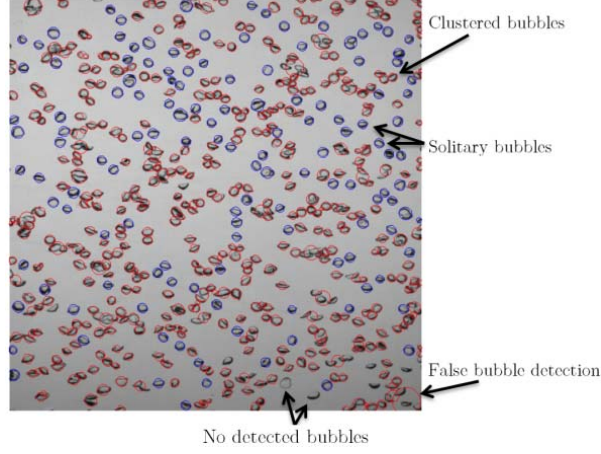


Figure 2.6: Bubble detection of clustered (red) and solitary (blue) bubbles by using the digital image analysis.
Configuration: $u_l=0$ mm/s, $u_g=10$ mm/s.

2.3 Particle image velocimetry

Particle image velocimetry is used to determine the local velocity of the bubbles in the pseudo-2D MSBC. The camera is focussed on the entire column and images are taken for a chosen amount of images. Two images with a short time difference (Δt) are coupled to produce a multi-frame image. The displacement of bubbles in this multi-frame image is calculated in areas of 32 by 32 pixels, which results in a vector field over the entire column for one multi-frame. If all these vector fields of the multi-frames are averaged locally, an overall result is presented. Figure 2.7 shows the result of one multi-frame and the averaged result of 5000 images.

The velocity is calculated by Equation 2.3. The displacement (Δx) over time (Δt) provides the velocity (u_b) in pixels per second, which is converted by image magnification factor (M) to SI units.

$$\overrightarrow{u_b(x, t)} = \frac{\overrightarrow{\Delta x(x, t)}}{M \cdot \Delta t} \quad 2.3$$

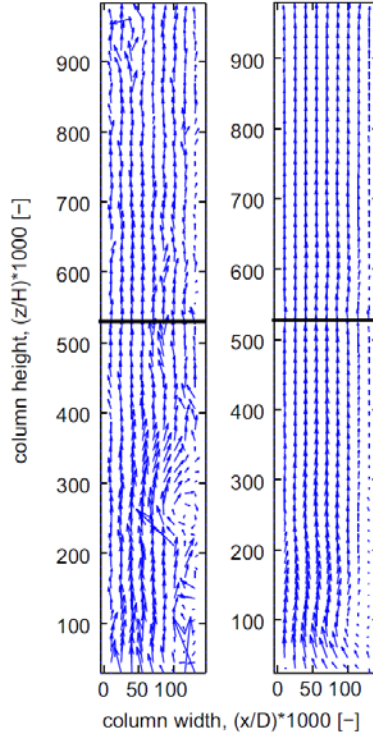


Figure 2.7: Two figures of the PIV technique, where on the left a single multi-frame and on the right the result of 5000 images are shown [2]. Configuration: wire-mesh openings of 3.7 mm, $u_g=15$ mm/s and $u_l=0$ mm/s.

Images are taken by a high speed camera at a distance of approximately 2 meters from the column, which ensures the entire column is captured. To obtain reliable results, 5000 images are recorded with a 50 Hz high speed camera. Post-processing of the images is performed by a LaVision program called DaVis, which result in the bubble velocities over the column.

2.4 Gas holdup

Gas holdup is measured by height reduction after shutting off liquid and gas supply simultaneously, see Equation 2.4. The height of the column during operation is known (h_r). After the gas and liquid supply are stopped simultaneously, the liquid level decreases until (h_l). The difference in height is caused by the gas holdup.

$$\varepsilon_g = \frac{h_r - h_l}{h_r} \quad 2.4$$

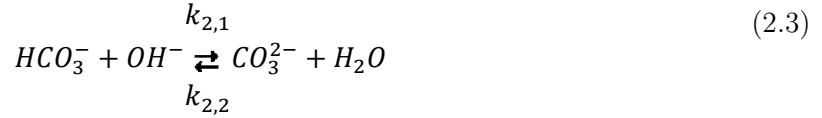
2.5 Chemisorption experiments

Chemisorption experiments are used to validate the tanks-in-series model explained in Chapter 4. The model describes the micro-structured bubble column for a reactive NaOH solution with CO₂ (pure) bubbles. This section explains the reaction kinetics, mass transfer and the procedure of these experiments.

Gas to liquid mass transfer is taking place by absorption, see reaction Equation (2.1).



When CO₂ is absorbed, only two elementary reactions are taken into account, which are shown by reaction Equation (2.2) and (2.3). Where $k_{1,1}$ and $k_{1,2}$ are the rate constants for the forward and $k_{2,1}$ and $k_{2,2}$ the rate constants for the backward reaction.



2.5.1 Reaction kinetics

Reaction kinetics are based on Darmana [1], who described detailed modelling of the reaction of NaOH with CO₂ using a discrete bubble model (DBM). Reaction rates for elementary reactions (2.2) and (2.3) are shown by Equation 2.5 to 2.8.

$$r_{1,1} = k_{1,1} \cdot [CO_2(aq)] \cdot [OH^-] \quad 2.5$$

$$r_{1,2} = k_{1,2} \cdot [HCO_3^-] \quad 2.6$$

$$r_{2,1} = k_{2,1} \cdot [HCO_3^-] \cdot [OH^-] \quad 2.7$$

$$r_{2,2} = k_{2,2} \cdot [CO_3^{2-}] \quad 2.8$$

The rate constant $k_{1,1}$ is calculated by Equation 2.9, from Pohorecki and Maniuk [15]. This relation is valid for the absorption of CO₂ into a pure NaOH solution varying from 0.1 to 4 M (molar) and a temperature range of 294-314 K.

$$\log \frac{k_{1,1}}{k_{1,1}^\infty} = 0.221 \cdot I - 1.6 \cdot 10^{-2} \cdot I^2 \quad 2.9$$

Where ionic strength (I) of the solution is given by

$$I = \frac{1}{2} \cdot \left([Na^+] \cdot z_{Na^+}^2 + [OH^-] \cdot z_{OH^-}^2 + [HCO_3^-] \cdot z_{HCO_3^-}^2 + [CO_3^{2-}] \cdot z_{CO_3^{2-}}^2 \right) \quad 2.10$$

Rate constant at infinite dilution is given by

$$\log k_{1,1}^\infty = 11.895 - \frac{2382}{T} \quad 2.11$$

Backward rate constant $k_{1,2}$ is calculated by the equilibrium constant K_1 . K_1 is calculated by Equation 2.12. This equation uses K_3 and K_W , which are represented by Equation 2.13 and 2.14 respectively.

$$K_1 = \frac{K_3}{K_W} = \frac{[HCO_3^-]}{[CO_2] \cdot [OH^-]} \quad 2.12$$

$$K_3 = \frac{[HCO_3^-] \cdot [H_3O^+]}{[CO_2]} = \exp\left(-\frac{12092.1}{T} - 36.786 \cdot \ln T + 235.482\right) \quad 2.13$$

$$K_W = [H_3O^+] \cdot [OH^-] = 10^{\left(-\frac{5839.5}{T} + 22.4773 \cdot \log T - 61.2062\right)} \quad 2.14$$

Finally the backward reaction ($k_{1,2}$) is calculated via Equation 2.15.

$$k_{1,2} = \frac{k_{1,1}}{K_1} \quad 2.15$$

The second reaction is based on results from Bhat et al. [16] who found that $k_{2,1}$ is in the order of 10^{10} to 10^{11} [$m^3 \text{mol}^{-1} \text{s}^{-1}$]. The equilibrium constant of reaction is determined from Näsänen and Kilpi [17].

$$\log K_2 = \log K_2^\infty + \frac{1.01\sqrt{[Na^+]}}{1 + 1.27\sqrt{[Na^+]}} + 0.125 \cdot [Na^+] \quad 2.16$$

Where the equilibrium constant at infinite dilution is defined as

$$\log K_2^\infty = \frac{1568.94}{T} + 0.4314 - 0.006737 \cdot T \quad 2.17$$

With K_2 from Equation 2.16, $k_{2,2}$ is calculated

$$k_{2,2} = \frac{k_{2,1}}{K_2} \quad 2.18$$

2.5.2 Physical absorption

Physical absorption of CO₂ into the NaOH solution is described by assuming that no reaction enhancement is present, as seen in Equation 2.19.

$$k_l a_b = \frac{k_l N_b \bar{A}_b}{V_l} = -\frac{1}{t} \ln \left(1 - \frac{CO_2^l}{H \cdot CO_2^g} \right) \quad 2.19$$

The mass transfer coefficient (k_l) is determined by the Sherwood correlation. The Sherwood correlation has the general form as is represented in Equation 2.20, where the factor 2 represent molecular diffusion. The other contribution in this formula is due to bubble swarms which contribute to the mass transfer. For this standard Equation, many different correlations have been derived. Different Sherwood correlations are compared in Appendix III. In this study, the equation of Brauer and Mewes is used. This correlation is proposed for ellipsoid bubbles taking into account the influence of deformation turbulence. The used coefficients in the Brauer and Mewes equation are: a=0.015, b=0.89 and c=0.7.

$$Sh = \frac{k_l^j d_b}{D^j} = 2.0 + a Re^b Sc^c \quad 2.20$$

2.5.3 Chemical enhancement

The contribution of chemical reaction to the mass transfer rate is described by the enhancement factor (E). This enhancement factor is defined as the ratio of absorption flux with chemical reaction to the absorption flux without chemical reaction for identical mass transfer driving force. The contribution of the enhancement factor to the mass transfer rate is displayed in equation 2.21.

$$N = E k_l N_b A_b (H \cdot CO_2^g - CO_2^l) \quad 2.21$$

Various approximations of this enhancement factor are available for different chemical reactions. Vladimir [18] studied the enhancement factor of the chemisorption of CO₂ into a NaOH solution. From this study, a correlation was proposed for the enhancement factor based on the pH of the solution by fitting parameters a, b, c and d, see Equation 2.22.

$$\frac{E_A - 1}{E_\infty - 1} = a \cdot \tanh(b \cdot Ha) + c \cdot \tanh(d \cdot Ha) \quad 2.22$$

Where the infinite enhancement is defined as

$$E_\infty = 1 + \frac{D_{OH^-} \cdot [OH^-]}{2D_{CO_2} \cdot [CO_2^g]} \quad 2.23$$

The values of a, b, c and d were found to be

$$a = 0.01219 pH^3 - 0.4248pH^2 + 4.952pH - 18.84 \quad 2.24$$

$$\log_{10} b = -0.1444pH^3 - 5.116pH^2 - 60.74pH + 241.5 \quad 2.25$$

$$c = -0.04397 pH^3 + 1.60449pH^2 - 19.4859pH + 79.18132 \quad 2.26$$

$$\log_{10} d = -0.06895pH^3 + 2.37848pH^2 - 28.2303pH + 114.279 \quad 2.27$$

Equations 2.24 to 2.27 were derived for alkaline solutions with a pH range from 10 to 14. For pH values lower than 10, it is known that enhancement is less active and is approaching unity. Therefore, these Equations are suitable for the studied pH range lower than 12.5.

2.5.4 Experiments procedure

Experiments are carried out in an alkaline solution with a pH of approximately 12.5. The alkaline solution is prepared and pumped into the bubble column and side vessel. The liquid is circulated and inert N₂ gas is fed. When the hydrodynamics inside the column are stable, the gas flow is switched to CO₂ and the reaction begins. During the reaction the pH and temperature are measured from the top of the reactor and logged. Gas holdup is checked at the end of the reaction by the height difference. Bubble sizes are measured over the entire column by the DIA technique. This is performed by dividing the column in 5 sections of each approximately 20 cm to maintain adequate resolution for bubble detection.

2.6 Tracer experiments

Tracer experiments are performed to gain more knowledge about the liquid phase behaviour for simulations. These experiments are performed by adding a salt solution and measuring the response at the outlet. The tracer experiments can be performed by a pulse or a step test. A pulse test is performed by injecting a small amount of concentrated salt solution at the inlet of the reaction. A step input test is performed by continuously adding tracer to the system. Step injection has the downside that the column needs to be drained and refilled every measurement. Another disadvantage is that more tracer solution is needed when using step injection. On the other hand, pulse injection requires a high response time. The conductivity meter (Scott, Model: GC855) used for experiments records every 0.02 seconds and this response time is sufficient for pulse injection. Therefore, pulse injection is preferred and implemented for these measurements.

Principle of tracer experiments

The E-function is used to approximate the liquid phase mixing in terms of a number of ideal continuous stirred tank reactors (CSTRs) in series (see Equation 2.28).

$$E = \frac{C(t)}{\int_0^\infty C(t) dt} \tag{2.28}$$

The E-function represents the concentration (conductivity) at a certain time over the total concentration. The integral of the E-function with respect to time is the fraction of concentration passed. Therefore, the integral of E from zero to infinity with respect to time is equal to unity, see Equation 2.29. Figure 2.8 represent an example of the E-function plotted versus time of 2 ideal CSTRs in series. The area below the graph from start to t=60, represents a fraction of 0.85 of the total injected concentration of tracer.

$$\int_0^\infty E(t) dt = 1 \tag{2.29}$$

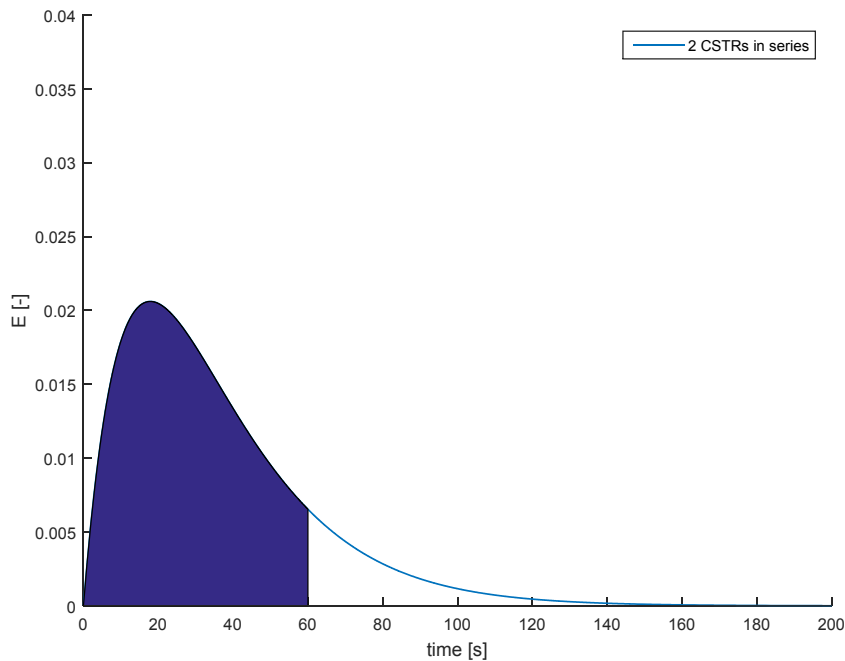


Figure 2.8: E-function versus time for the 2 ideal CSTRs in series. The filled area represents the fraction of concentration passed. In this case at 60 seconds a fraction of 0.85 of the total concentration has passed the measurement point.

Experimental setup and measurement techniques

From E-curves, the mean residence time and variance are calculated by Equation 2.30 and 2.31 respectively. These parameters are used to calculate the number of ideal CSTRs in series required to model the liquid mixing in a MSBC by Equation 2.32.

$$t_m = \frac{\int_0^{\infty} t \cdot E(t) dt}{\int_0^{\infty} E(t) dt} = \int_0^{\infty} t \cdot E(t) dt \quad 2.30$$

$$\sigma^2 = \int_0^{\infty} (t - t_m)^2 \cdot E(t) dt \quad 2.31$$

$$N_{CSTR} = \frac{t_m^2}{\sigma^2} \quad 2.32$$

3 Experimental results

The results are first analysed by a visual observation, followed by a detailed hydrodynamic study. The visual observation screens the available structured packings for different gas and liquid velocities. This screening yields the parameter space in which bubble cutting is visible. This parameter space is studied in more detail in the hydrodynamic study. After this study, the results of the performed tracer experiments are discussed, which derive the liquid mixing as a number of ideal CSTRs. This obtained behaviour of the liquid phase is used for the modelling of the MSBC.

3.1 Visual observation

The visual observation is performed to examine the phenomena occurring inside the column and observe cutting behaviour of different structured packings. These experiments are also used to check if the analysis performed by DIA is able to detect the bubbles. The result of this screening is used to determine the parameter space for detailed experiments in the hydrodynamic study.

Two types of structured packings are studied: wire-meshes and a Sulzer packing, which can be seen in Figure 3.1. The Sulzer packing has a more closed structure and occupies more volume than the meshes. The configuration of the four wire-meshes defined by wire diameters, mesh openings and open areas are different. Table 3.1 illustrates the parameters for the available wire-meshes.

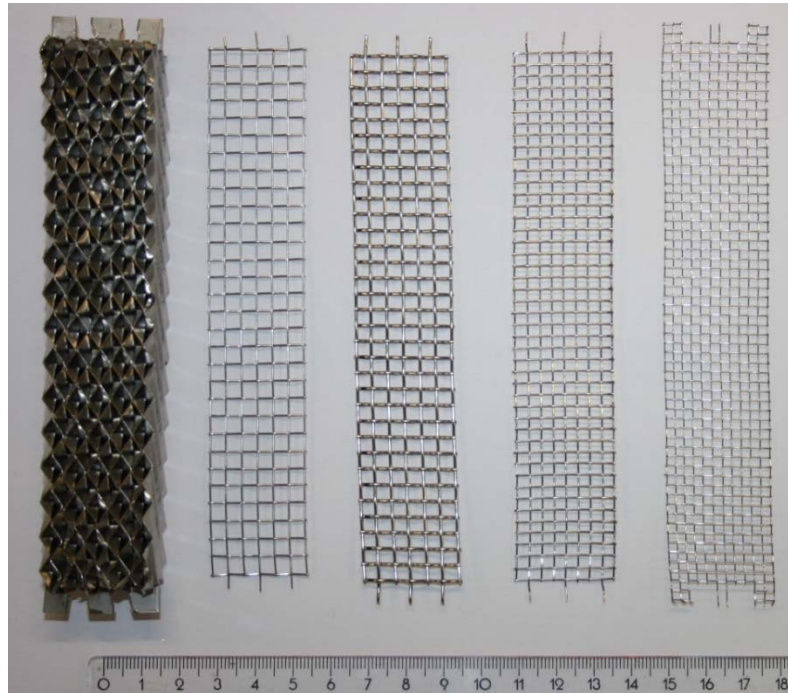


Figure 3.1: Types of packing. From left to right: Sulzer packing, wire-mesh openings of 3.6, 3.3, 2.7 and 2.2 mm.

Table 3.1: Parameters of the investigated wire-meshes.

Wire diameter [mm]	Wire-mesh openings [mm]	Open area [%]
0.55	3.6	76
0.90	3.3	62
0.50	2.7	71
0.31	2.2	75

Experiments for different gas and liquid velocities are performed for every packing. The upper limit of superficial liquid velocity is based on the maximum capacity of the available pump: 28 mm/s. Furthermore, the maximum gas velocity is set to 30 mm/s, because the performance of DIA is decreasing significantly, around this velocity [14]. The chosen screening ranges of these velocities are:

- Superficial gas velocity: 5, 10, 15, 20, 25 and 30 [mm/s]
- Superficial liquid velocity 0, 7, 14, 21 and 28 [mm/s]

Categorization: The observed cutting behaviour is categorised into 4 phenomena. The phenomena's are shown in Figure 3.2 and categorized by colour markings as shown in Table 3.2.

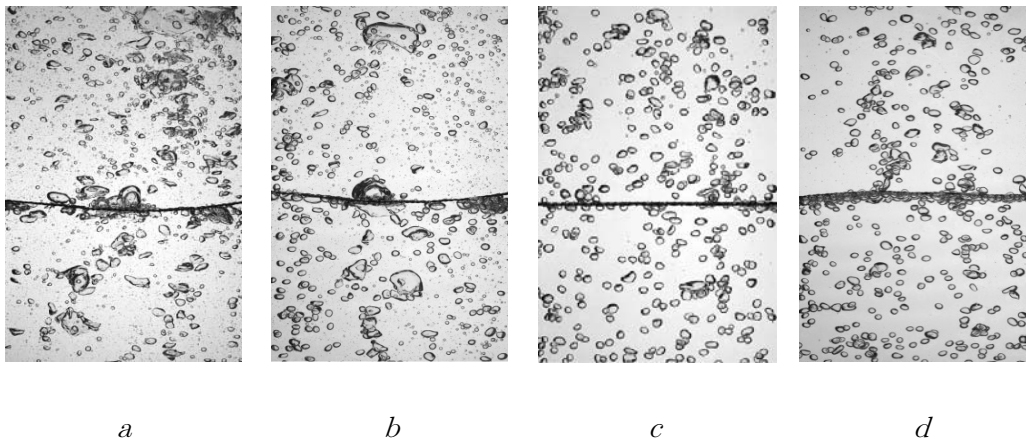


Figure 3.2: Four categorized phenomena observed during visual observation, a more detailed description with colour coding of the different phenomena is given in Table 3.2.

The first image shows the desired phenomena (Figure 3.2a), where most bubble are cut and small bubbles are observed above the mesh. The second image shows some bubbles retained on the sides. Big bubbles are cut but mostly re-coalesce after the mesh, as shown in Figure 3.2b. Figure 3.2c shows that no significant cutting is observed in this homogeneous regime. The last categorized phenomena is the gas cushion observation below the wire-mesh, see Figure 3.2d. The gas cushion is undesirable since it causes the bubbles to by-pass the mesh at the walls and enhances the re-coalescence of bubbles after the mesh [6].

Table 3.2: Cutting behaviour categorized into four observed phenomena with colour markings corresponding to in Figure 3.2.

<i>Label in Figure 3.2</i>	<i>Cutting behaviour</i>	<i>Colour marking</i>
<i>a</i>	<i>Most bubbles get cut by the wire-mesh.</i>	Green
<i>b</i>	<i>Big bubbles flow through wire-mesh but mostly re-coalesce after mesh, some bubbles are retained at the sides, cutting occurs.</i>	Yellow
<i>c</i>	<i>Bubbles flow through mesh, some cutting.</i>	Blue
<i>d</i>	<i>Formation of gas-cushion. Bubbles accumulate below the mesh. By-passing and re-coalesce of bubbles observed.</i>	Red

3.1.1 Results

The phenomena in the MSBC are represented in tables by using the colour coding according to Table 3.2. Table 3.3 and Table 3.4 represent the results for superficial liquid velocity 0 and 28 mm/s respectively (additional tables are added to Appendix I). These tables display that the influence of liquid velocity on the phenomena observed inside the column is relatively small. The change from blue to green (for Sulzer, mesh 3.6 and 3.3 at $u_g=10$ to 15 mm/s) is probably caused by the shift of flow regime from homogeneous to transition regime. Therefore, bubbles are larger in size and bubble cutting is becoming more active. Gas cushions are observed at the mesh with smallest openings (2.2 mm) at low gas velocities. Another observation is that small bubbles (green) are observed more frequently at higher gas velocities. This might be caused by bubble cutting, but requires a more detailed study to define the cutting of bubbles at different gas velocities.

Table 3.3 Results visual observation, $u_l=0$ mm/s.

$u_l=0$ [mm/s]		u_g [mm/s]					
		5	10	15	20	25	30
Wire-mesh/ Packing	Sulzer	Blue	Blue	Green	Green	Green	Green
	3,6	Blue	Blue	Green	Green	Green	Green
	3,3	Blue	Blue	Green	Green	Green	Green
	2,7	Blue	Yellow	Green	Green	Green	Green
	2,2	Red	Red	Yellow	Green	Green	Green

Table 3.4: Results visual observation, $u_l=28$ mm/s.

$u_l=28$ [mm/s]		u_g [mm/s]					
		5	10	15	20	25	30
Wire-mesh/ Packing	Sulzer	Blue	Blue	Green	Green	Green	Green
	3,6	Blue	Blue	Green	Green	Green	Green
	3,3	Blue	Blue	Green	Green	Green	Green
	2,7	Blue	Blue	Blue	Green	Green	Green
	2,2	Red	Red	Yellow	Green	Green	Green

3.1.2 Chosen parameter space for hydrodynamic study

Based on the visual observation it is chosen to investigate two wire-meshes and the Sulzer packing in a detailed hydrodynamic study. From previous study with the same meshes, it has been found that 3.6 mm mesh has the best performance [13] and is included in the hydrodynamic investigation. Mesh 2.7 mm is also included since it has a comparable wire diameter. Therefore, a comparison can be made between these two meshes based on the difference in mesh opening.

At highest gas velocity (30 mm/s), DIA had already significant difficulty with the detection of bubbles. Due to the relatively high gas holdup, the algorithm has difficulties to distinguish between background and bubbles. Therefore, the gas velocity parameters space was limited to a maximum of 25 mm/s. At relatively low gas velocity (5 mm/s) no significant cutting was observed. The gas and liquid superficial velocity parameter space was chosen as follows:

- Superficial gas velocity: 10, 15, 20 and 25 mm/s
- Superficial liquid velocity: 0, 7, 14 and 28 mm/s

The results of the hydrodynamic study are discussed in the next section.

3.2 Hydrodynamic study

In this section, the influence of liquid velocity on cutting behaviour, bubble velocity and gas holdup are shown. This is investigated by varying internal structures, superficial gas and liquid velocities, corresponding to the parameter space derived by visual observation. These internal structures are used to cut the bubbles and improve the specific surface area, resulting in increased mass transfer rates. During this hydrodynamic study, DIA technique is used to track bubble diameter in the region near the mesh (± 22 cm). The bubble diameter is displayed over the height of the column near the mesh, to see the influence of bubble cutting (reduction in bubble size). Additionally, the bubble diameter is represented in the form of a bubble size distribution, which indicates the number amount of bubbles present in a certain size class. Bubble velocities are calculated over the column by using a bubble PIV technique.

Since the results from the DIA technique detect a distribution of bubble sizes, a proper representations of the bubble diameter is needed. Therefore, diameters of the bubbles are presented in two forms: a) number mean diameter (d_{10}) or b) Sauter mean diameter (d_{32}). The diameters are defined as given by Equation 3.1 and 3.2.

$$d_{10} = \frac{\sum_1^n d}{n} \quad 3.1$$

$$d_{32} = \frac{\sum_1^n d^3}{\sum_1^n d^2} \quad 3.2$$

The number mean diameter (d_{10}) can quantify the cutting of the bubbles and the contribution of large and small bubbles are equal in this diameter. The Sauter mean diameter is more obvious to use when mass transfer needs to be quantified. Since this diameter is based on the volume to surface area ratio, bigger bubbles have a more significant contribution. Since small bubbles need

to be in larger numbers to be significant in the Sauter mean diameter. Therefore, the Sauter mean diameter is larger than number mean diameter.

In this Chapter mostly the Sauter mean diameter is used to evaluate bubble size reduction due to cutting of bubbles. Due to the number mean diameter being overruled by the amount of small bubbles (<1.2 mm) and results in less representative graphs. Therefore, if the number mean diameter is used to show cutting, these bubbles (<1.2 mm) are left out of consideration.

Two different probability functions are used for displaying the distribution of bubble sizes in the bubble column. These are the probability density function (PDF) and the volumetric probability density (VPD). Both probability densities are based on ordering bubble sizes, where bubbles of similar diameter are placed in the same bin. The PDF is based on the number of bubbles within a certain bin width divided by the total number of bubbles, which is multiplied by the reciprocal bin width, see Equation 3.3. The PDF gives an indication of the amount of present bubbles of each class. The VPD observes how the bubbles within a bin contribute to the gas holdup. This is done by multiplying the PDF by the ratio of volume in the bin over the average total volume, see Equation 3.4.

$$PDF = \frac{\sum_{i=1}^{bin} n}{\sum_{i=1}^{total} n} \cdot \frac{1}{d_{bin}} \quad 3.3$$

$$VPD = PDF \cdot \frac{\overline{V_{bin}}}{\overline{V_{total}}} \quad 3.4$$

3.2.1 Influence of liquid velocity

Figure 3.3 and Figure 3.4 depicts the influence of liquid velocity on bubble size in the middle of the column. It shows that in all configurations the diameter slightly decreases over the height of the column. Furthermore, increasing the superficial liquid velocity results in a larger bubble diameter. Interestingly, a superficial liquid velocity of 28 mm/s has a lower number mean diameter (d_{10}) than the 14 mm/s case, which indicates the presence of more small bubbles. However, this difference is barely noticeable when looking at Sauter mean diameter (d_{32}). A possible explanation for this is that there is a change in break-up and coalescence behaviour from liquid velocities of 14 to 28 mm/s.

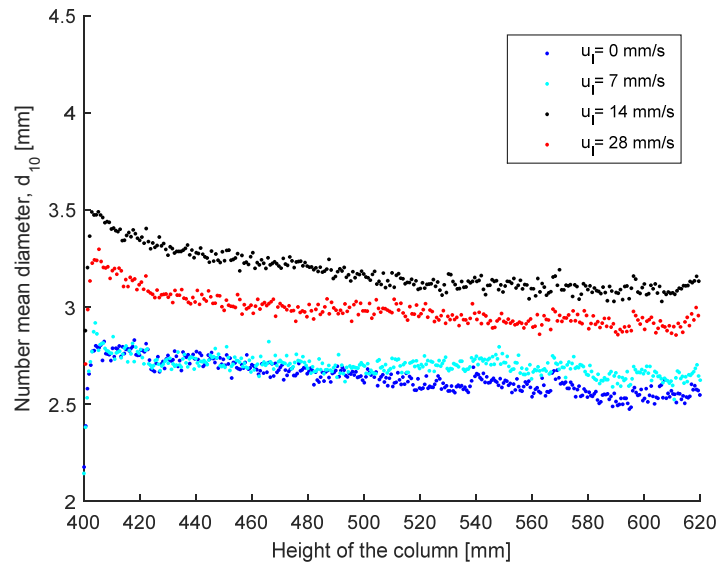


Figure 3.3: Number mean diameter (d_{10}) over middle section column at different liquid velocities. At 400 mm, some side effects of the detection are visible. Configuration: no wire-mesh, $u_g = 20$ mm/s, $u_l = \text{variated}$.

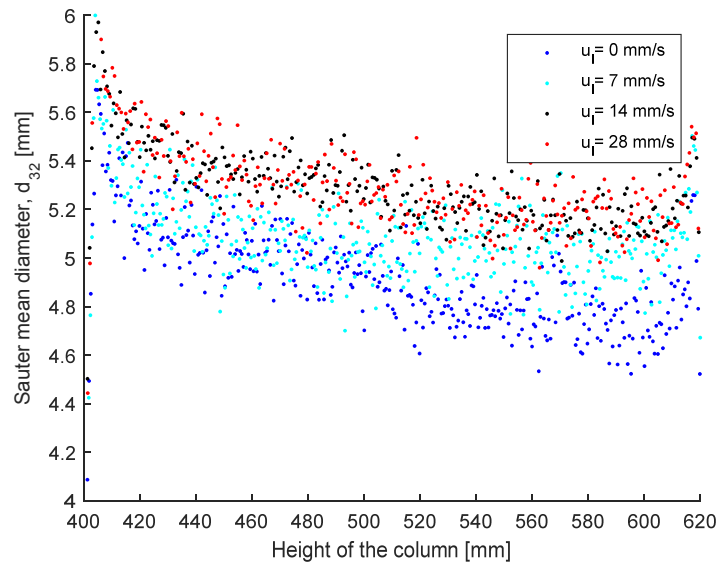


Figure 3.4: Sauter mean diameter for different liquid velocities over the middle section of column. At the 400 and 620 mm, some side effects of the detection are visible. Configuration: no wire-mesh, $u_g = 20$ mm/s, $u_l = \text{variated}$.

The difference in bubble diameter between the two high liquid velocities ($u_l = 14$ and 28 mm/s) is supported by the volumetric probability density function (see Figure 3.5). Liquid velocity of 14 mm/s shows the least density of small bubbles (1.2 to 4 mm) and the highest peak around 5.5 mm. Furthermore, exerting liquid velocity resulted in less small bubbles present. This might be due to the fact that liquid flow drags the small bubble along with the flow. Normally, when there is no liquid velocity, small bubbles have a low rise velocity. The exertion of liquid velocity seems to increase the rise velocity and results in less activity of small bubbles. Moreover, at higher bubble diameter (>8 mm), liquid velocity decreases the amount of big bubbles, which seem to be caused because of a shift of bubble breakup and coalescence inside the column.

Overall, liquid velocity seem to shift the bubble diameter to a more uniform size, around 5.5 mm. Similar results are also found at low gas velocity (10 mm/s), as shown in Appendix II.

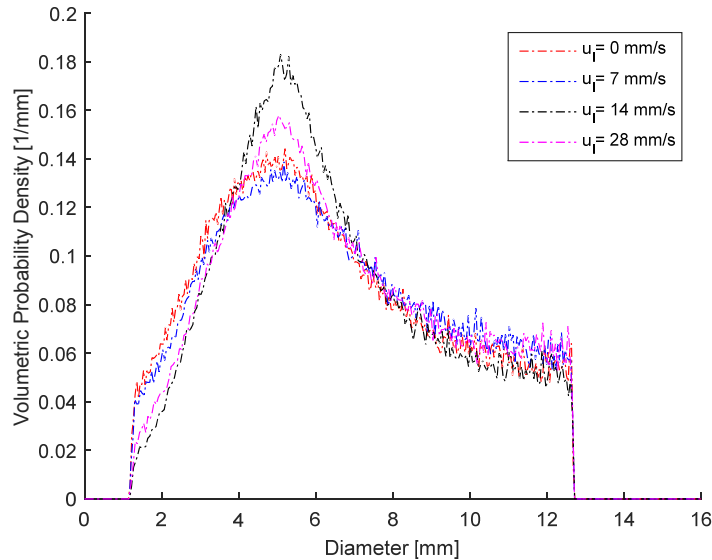
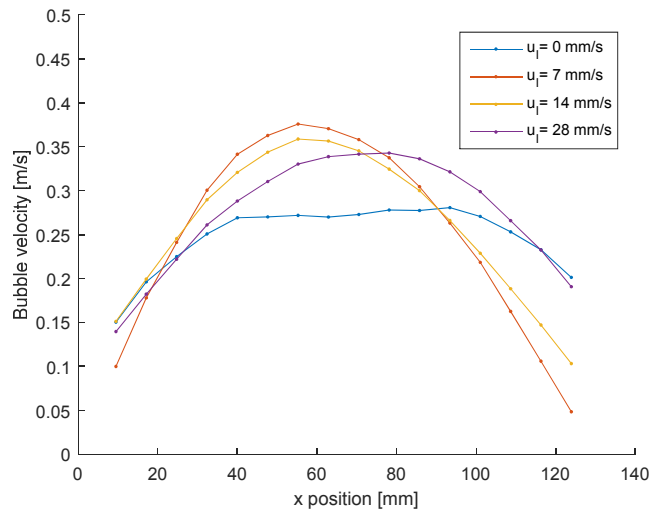


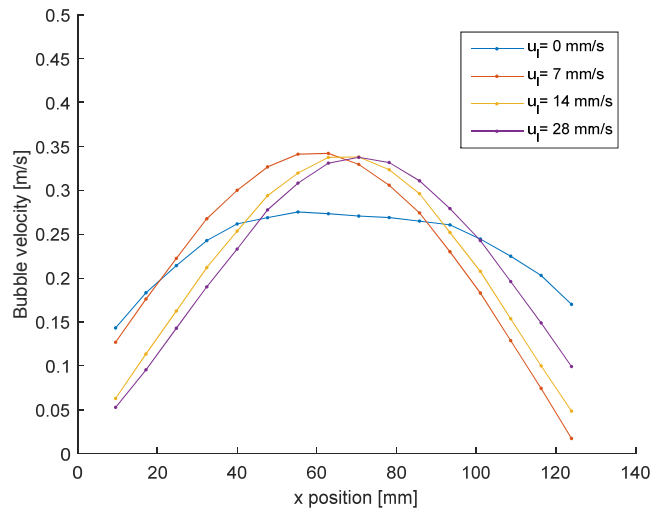
Figure 3.5: Volumetric probability density for different liquid velocities. The graph is cut-off at the minimal and maximum bubble diameter, discussed with the DIA technique (section 2.2).

Configuration: no wire-mesh, $u_g = 20$ mm/s, $u_l = \text{variated}$.

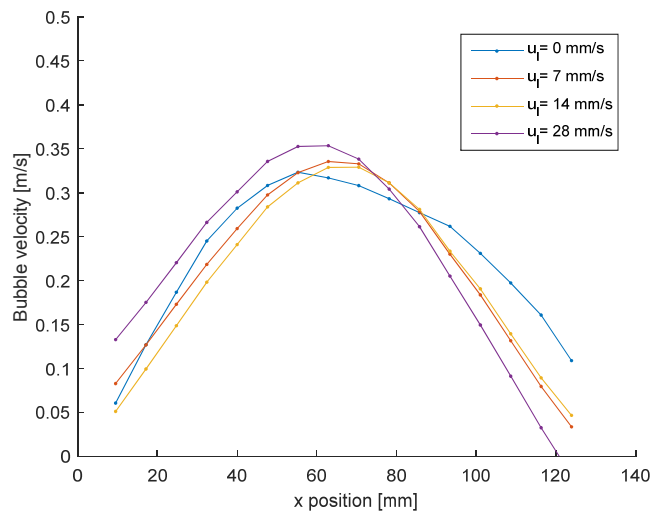
The results from PIV experiments show the influence of superficial liquid velocity on bubble velocity inside the reactor. Figure 3.6 depicts the bubble velocity profiles in x-direction for different liquid velocities at different heights in the column. Figure 3.6a displays the velocity profile at the inlet of the column. The configuration without liquid velocity shows significantly lower bubble velocity in the beginning of the column. The configuration with no liquid velocity shows a lower gas velocity in the middle of the column, as Figure 3.6b depicts. At the top section (see Figure 3.6c) the bubble velocities of all configurations are similar. This means that at the top part of the column, the influence of liquid velocity on bubble velocity is decreasing. In the beginning the contribution of low liquid velocity (7 mm/s) increases the bubble rise velocity significantly, which might be due to the decreasing drag force. No significant difference in bubble velocity is observed from a liquid velocity of 7 to 28 mm/s. This might indicate that there is a maximum rise velocity that does not increase further when superficial liquid velocity is increased.



a



b



c

Figure 3.6: Bubble velocity profiles over the width (x -direction) of the column. (a): inlet (18 cm), (b): middle position (52 cm) and (c): outlet of the column (82 cm). Configuration: no wire-mesh, $u_g = 20$ mm/s, $u_i = \text{variated}$.

3.2.2 Influence of structured packings

Previous section showed that the number mean diameter was significantly influenced by the small bubbles (>3 mm). These small bubbles are not of interest in bubble cutting, therefore, the number mean diameter is not used for quantifying the bubble cutting. The Sauter mean diameter is more representative for showing the influence of the mesh on the cut larger bubbles (± 5 mm). Figure 3.7 depicts the Sauter mean diameter for different internal configurations. This configuration shows that the wire-meshes reduces the bubble size most significantly due to bubble cutting. Sulzer packing seem to have a similar or even higher bubble diameter than the no mesh case.

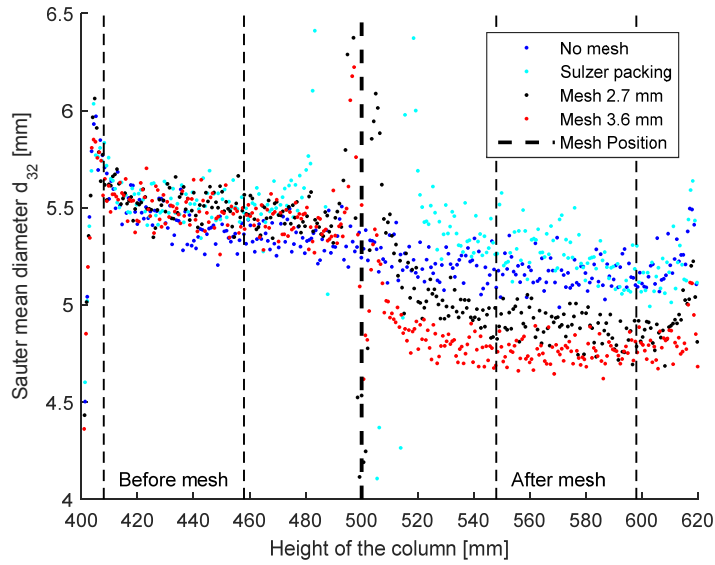


Figure 3.7. Sauter mean diameter over middle section column. Configuration: different internal configurations, $u_g=20$ mm/s, $w_l=14$ mm/s.

To quantify the cutting for all configurations, a cutting difference is proposed by Equation 3.5. The region before and after mesh are also indicated in Figure 3.7.

$$\Delta d_{32} = \langle d_{32}^{before} \rangle - \langle d_{32}^{after} \rangle \quad 3.5$$

Equation 3.5 is used to indicate the influence of superficial liquid velocity on bubble cutting. Figure 3.8 represents the cutting performance for different superficial liquid velocities. Increasing superficial liquid velocity resulted in no significant enhancement of bubble cutting. Mesh 3.6 mm had the most significant cutting performance. Remarkably, Sulzer packing had a low cutting performance and even decrease towards the no mesh case with increasing liquid velocity.

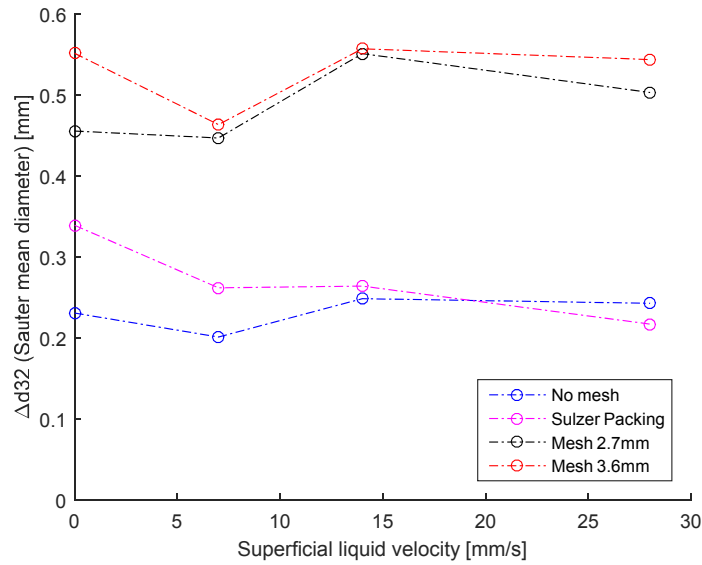


Figure 3.8: Influence of superficial liquid velocity on bubble cutting. Configuration: different internal configurations, $u_g=20$ mm/s, u_l =variated.

Lower cutting results of Sulzer packing are also observed by the VPD shown in Figure 3.9. When using Sulzer packing, the activity of big bubbles (>8 mm) is higher and the peak of the most active bubbles is smaller at ± 5.5 mm. On the other hand, Mesh 3.6 mm showed a shift of big bubbles (>8 mm) to smaller bubbles (2-6 mm) compared to the no mesh case.

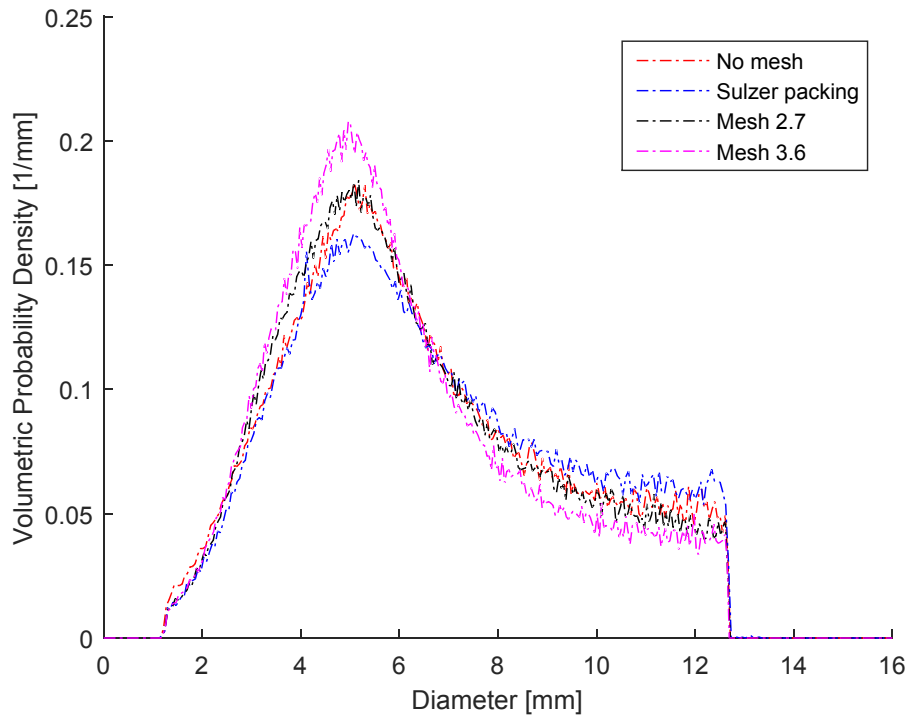


Figure 3.9: VPD for comparing different internal configurations. Configuration: different internal configurations, $u_g=20$ mm/s, $u_l=14$ mm/s.

Figure 3.10 depicts the velocity profile before and after the different internal configurations. It shows that all internals decrease the bubble velocity significantly. The meshes have a slightly higher bubble velocity compared to the Sulzer packing. This difference in bubble velocity might causes more force for cutting the bubble and could possibly explain why Sulzer packing has lower cutting results.

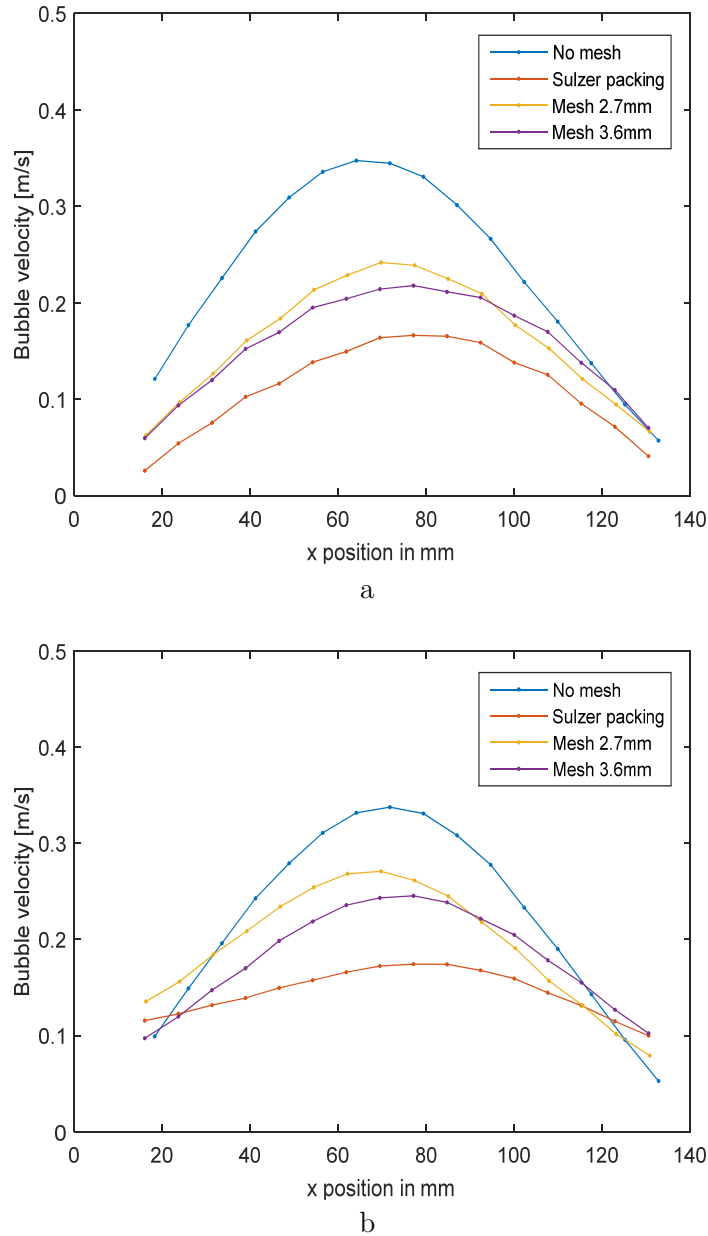


Figure 3.10: Radial bubble velocity profiles comparison. (a): before mesh (48 cm) and (b): after mesh (52cm). Configuration: different internal configurations, $u_g=20$ mm/s, $u_l=28$ mm/s.

Gas holdup was expected to decrease with increasing liquid velocity, as discussed in section 1.3. It is measured to see the influence of every configuration on the amount of gas present in the column. During the experiments, it was found that the measurement error of the gas holdup was quite significant. Therefore, the differences in gas holdup between the structured packings was not measurable with this technique. This was caused due to the practical problem that the

gas and liquid feed need to be stopped simultaneously, by manually shutting down both valves. However, the measured gas holdup without an internal structure is discussed to have a basic understanding of the influence of liquid velocity on the gas holdup.

Figure 3.11 represents the gas holdup dependency on superficial liquid velocity for the no mesh case. All lines show the same trend: gas holdup decreases with increasing liquid velocity. The gas holdup decreases most significantly from superficial liquid velocity 0 to 7 mm/s. Increasing the superficial liquid velocity from 7 to 14 and 28 mm/s, reduced the gas holdup less significantly. This result coincides with the result of the bubble velocity of Figure 3.10. Bubble velocity increased when low liquid velocity (7 mm/s) is exerted and further increase of liquid velocity did not result in a significant higher bubble velocity.

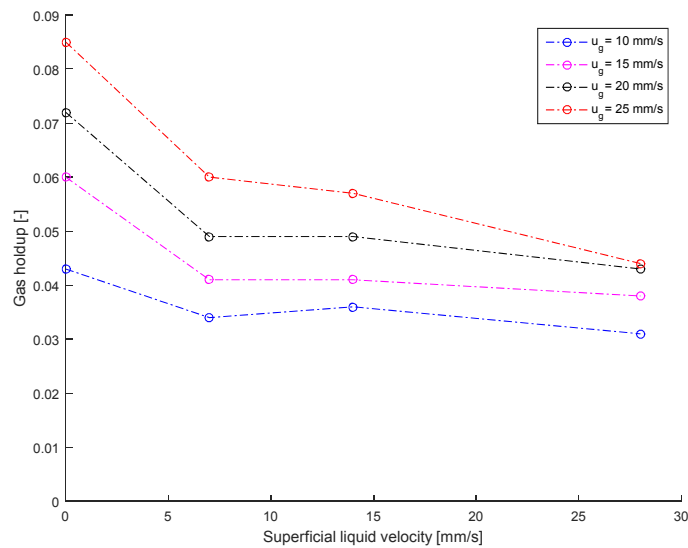


Figure 3.11: Gas holdup dependency on superficial liquid velocity. Configuration: no wire-mesh, u_g =variated, u_l =variated.

3.3 Results tracer experiments

This section discusses the results of the tracer experiments, which are a preliminary study for the CSTRs in series model of Chapter 4. A proper description of the liquid phase inside the bubble column is essential for the model, which can be provided by tracer experiments. These tracer experiments result in the liquid behaviour in an amount of CSTRs in series that is implemented in the model. Experiments are performed for gas velocities of 10 and 20 mm/s and liquid velocities of 7, 14 and 28 mm/s. These velocities are investigated for three insert configurations: no mesh, mesh 3.6 mm and Sulzer packing.

E-curves of the 3 different internal configurations are plotted for the high gas flow (20 mm/s) with the addition of the 1 and 2 ideal CSTR(s) curves as a comparison. Figure 3.12, Figure 3.13 and Figure 3.14 represents the E-curves for liquid velocity 7, 14 and 28 mm/s respectively.

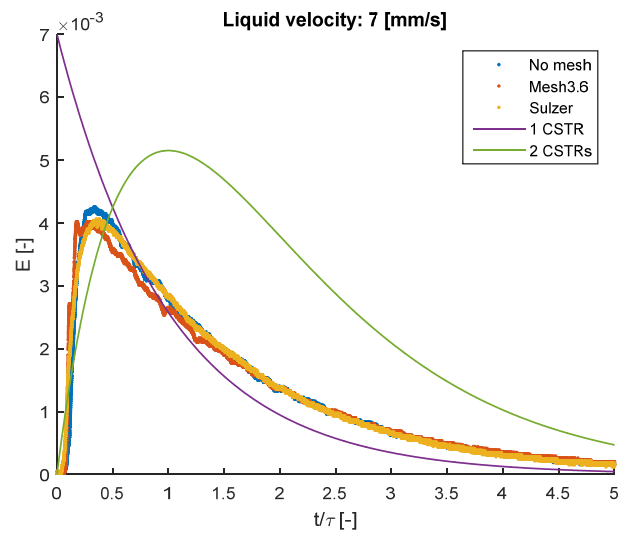


Figure 3.12: E-curves no mesh, mesh 3.6 mm and Sulzer packing and 1 and 2 ideal CSTR(s). Configuration: different internal configurations, $u_g=20$ mm/s, $u_l = 7$ mm/s.

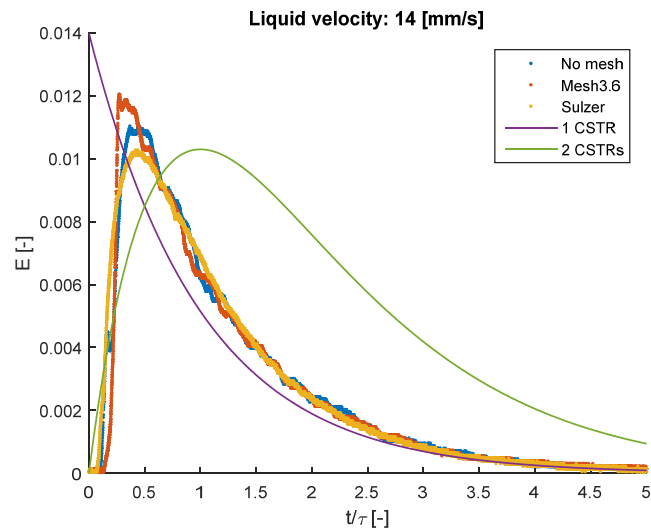


Figure 3.13: E-curves no mesh, mesh 3.6 mm and Sulzer packing and 1 and 2 ideal CSTR(s). Configuration: different internal configurations, $u_g=20$ mm/s, $u_l = 14$ mm/s.

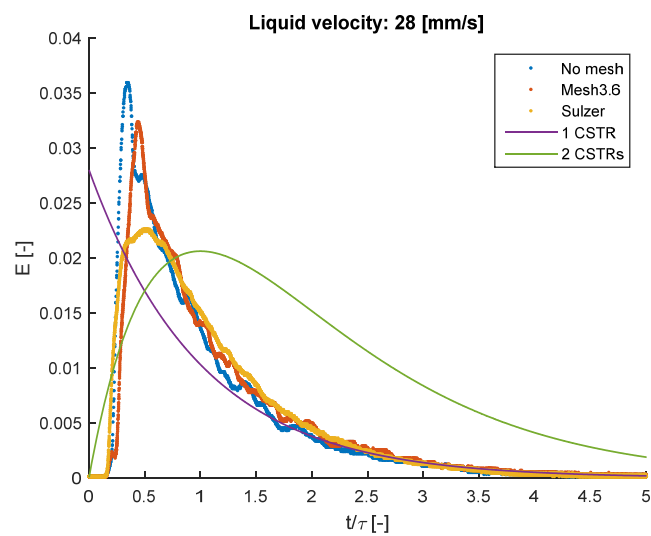


Figure 3.14: E-curves no mesh, mesh 3.6 mm and Sulzer packing and 1 and 2 ideal CSTR(s). Configuration: different internal configurations, $u_g=20$ mm/s, $u_l = 28$ mm/s.

Experimental results

The E-curves of Figure 3.12, Figure 3.13 and Figure 3.14 show that the behaviour of the column should be simulated as 1 to 2 ideal CSTR(s) for all internals. This is also seen when N_{CSTR} is calculated, see Table 3.5. In all instances, the behaviour is between one and two CSTRs in series. When a lower gas velocity (10 mm/s) is used, N_{CSTR} is found to be in the same range. On rounding off to integers, the liquid mixing behaviour inside the MSBC is represented by two CSTRs in series. In total the liquid phase consist of three ideal CSTRs in series, since the side vessel is simulated as an ideal CSTR as well.

Table 3.5: Number of CSTRs in series for each configuration (N_{CSTR}).

<i>Liquid velocity</i>	<i>7 [mm/s]</i>	<i>14 [mm/s]</i>	<i>28 [mm/s]</i>
No mesh	<i>1,40</i>	<i>1,67</i>	<i>1,64</i>
Mesh 3.6 mm	<i>1,21</i>	<i>1,32</i>	<i>1,63</i>
Sulzer packing	<i>1,36</i>	<i>1,57</i>	<i>1,92</i>

4 Modelling micro-structured bubble column

Hydrodynamics of bubbles in the MSBC with liquid circulation were studied in section 3.2. These experiments were all performed in a nonreactive air-water system. In this Chapter the description of the reactive system of CO_2 and NaOH is given. This model is used to model and validate the MSBC by experiments. This gives more understanding in how liquid flow influences the performance of the bubble column reactor and also shows how the side vessel influences the bubble column.

4.1 Model description

The gas and liquid phase are both divided into a certain amount of ideal continuous stirred tank reactors (CSTR). This is a simple model but it is sufficient to describe the MSBC and validate its behaviour. Figure 4.1 depicts the schematic representation of the bubble column. The liquid phase is modelled as three CSTRs (BC1, BC2 and V1), which resulted from tracer experiments (section 3.3). Where compartment BC1 and BC2 have interaction with the gas phase. The gas phase is simulated as a plug flow reactor with 100 CSTRs in series and an inlet condition ($z=1$). The amount of gas compartments ($NZ=101$) can be reduced to increase the effect of axial dispersion. The wire-mesh is located in the middle of the column between gas compartment 51 and 52. This figure additionally illustrates five different sections over the column on the right side of the liquid phase. These are the schematic regions of imaging for measuring the bubble sizes with the DIA technique. A slight overlap (2 cm) in the sections is chosen to check the data connectivity between the sections.

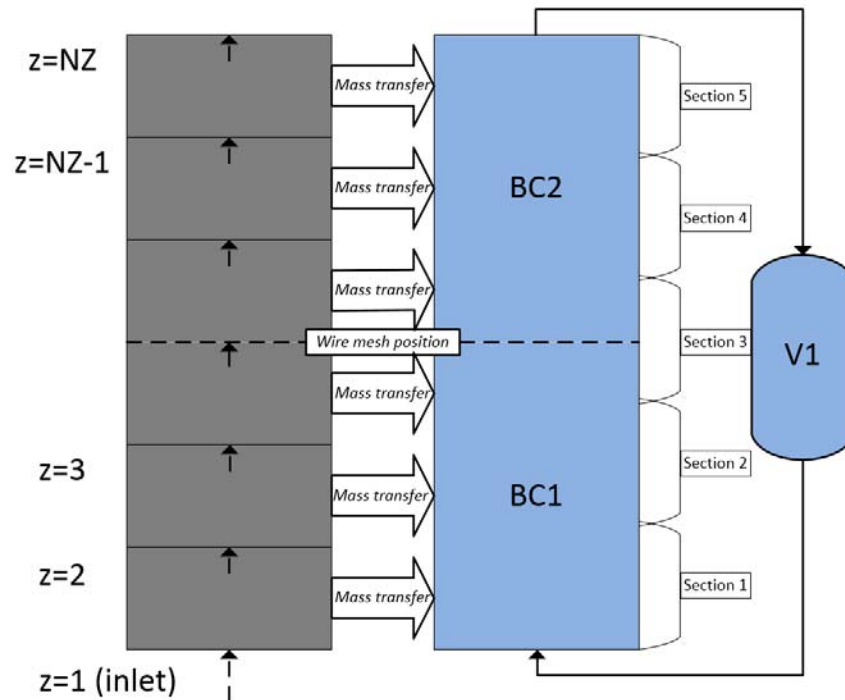


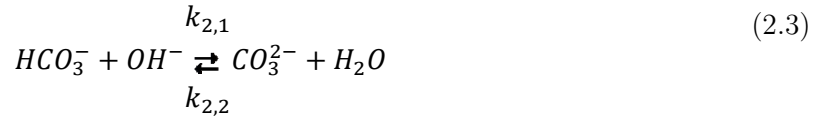
Figure 4.1: Schematic representation of the linkage between liquid and gas compartments for modelling the MSBC as a CSTRs in series model. Sections of the image recording for DIA is schematically shown next to the side vessel.

4.2 Balances

The balances for liquid and gas compartments and the linkage between these two phases are discussed in this section.

4.2.1 Liquid phase

As previously discussed in section 2.5, the two step liquid reactions of dissolved CO₂ in an aqueous NaOH solution, are displayed by reaction equation (2.2) and (2.3). These reactions are significantly fast, therefore, the rate controlling step is the gas-liquid mass transfer of CO₂.



Equations 4.1 to 4.4 represent the balances of the four components taken into account for this system, which are solved for every time (t). The general liquid balances for all three compartments are given with the code *X*, which could be BC1, BC2 or V1. Furthermore, the liquid velocity is calculated by the ratio between superficial liquid velocity and the liquid holdup (see Equation 4.5).

$$\frac{d[CO_2]^X}{dt} = u_l \cdot \frac{A^X}{V^X} \cdot ([CO_2]^{X-1} - [CO_2]^X) + MT^{X*} - r_{1,1}^X + r_{1,2}^X \quad 4.1$$

$$\frac{d[OH^-]^X}{dt} = u_l \cdot \frac{A^X}{V^X} \cdot ([OH^-]^{X-1} - [OH^-]^X) - r_{1,1}^X + r_{1,2}^X - r_{2,1}^X + r_{2,2}^X \quad 4.2$$

$$\frac{d[HCO_3^-]^X}{dt} = u_l \cdot \frac{A^X}{V^X} \cdot ([HCO_3^-]^{X-1} - [HCO_3^-]^X) + r_{1,1}^X - r_{1,2}^X - r_{2,1}^X + r_{2,2}^X \quad 4.3$$

$$\frac{d[CO_3^{2-}]^{BC}}{dt} = u_l \cdot \frac{A^X}{V^X} \cdot ([CO_3^{2-}]^{V1} - [CO_3^{2-}]^{BC}) + r_{2,1}^X - r_{2,2}^X \quad 4.4$$

$$u_l^{t-1} = \frac{u_l^{sup}}{\varepsilon_{l,tot}^{t-1}} = \frac{u_l^{sup}}{1 - \varepsilon_{g,tot}^{t-1}} \quad 4.5$$

The mass transfer terms corresponding to the linkage between the gas and liquid compartments BC1 and BC2 are shown by Equations 4.6 and 4.7.

* Mass transfer (*MT*) is only active in BC1 and BC2

$$MT^{BC1} = \frac{1}{V^{BC1}} * (H^{BC1} \cdot CO_2^g - [CO_2]^{BC1}) \cdot \sum_{i=2}^{(NZ+1)/2} N_b^{i,t-1} \cdot k_l^{i,t-1} \cdot A_b^{i,t-1} \cdot E^{i,t-1} \quad 4.6$$

$$MT^{BC2} = \frac{1}{V^{BC2}} * (H^{BC2} \cdot CO_2^g - [CO_2]^{BC2}) \cdot \sum_{i=((NZ+1)/2+1)}^{NZ} N_b^{i,t-1} \cdot k_l^{i,t-1} \cdot A_b^{i,t-1} \cdot E^{i,t-1} \quad 4.7$$

4.2.2 Gas phase

The gas phase system consists of pure CO₂ and, therefore, the concentration is constant. Parameters such as gas velocity (u_g), gas holdup (ε_g) and number of bubbles in a gas compartment (N_b) change with respect to position (z) and the time (t).

Gas velocity

Gas velocity is determined by the bubble rise velocity with the contribution of liquid flow, see Equation 4.8.

$$u_g^{z,t} = u_{bubble\ rise}^{z,t-1} + u_l^{t-1} \quad 4.8$$

Bubble rise velocity is dependent on the bubble diameter and drag coefficient (Equation 4.9). The drag correlation proposed by Tomiyama [19] (Equation 4.10) is based on a single bubble rising in a contaminated fluid.

$$u_{bubble\ rise}^{z,t-1} = \frac{1}{C_d} \cdot \frac{4 \cdot (\rho_l - \rho_g) \cdot g \cdot d_b^{z,t-1}}{3 * \rho_l} \quad 4.9$$

$$C_d = \max \left[\left(\frac{24}{Re} (1 + 0.15 \cdot Re^{0.687}) \right), \left(\frac{8}{3} \cdot \left(\frac{Eo}{Eo + 4} \right) \right) \right] \quad 4.10$$

Gas holdup

Gas holdup (ε_g) is calculated via Equation 4.11, which is a balance based on the in- and outflow of gas and mass transfer from the gas to the liquid phase.

$$\begin{aligned} \frac{\partial(CO_2^g \cdot \varepsilon_g^z \cdot V_{CSTR})}{\partial t} &= A_{BC} \cdot CO_2^g \cdot (\varepsilon_g^{z-1,t} \cdot u_g^{z-1,t} - \varepsilon_g^{z,t} \cdot u_g^{z,t}) - (H_{BC1/BC2} \cdot CO_2^g - [CO_2]_{BC1/BC2}^{t-1}) \\ &\cdot N_b^{z,t-1} \cdot k_l^{z,t-1} \cdot A_b^{z,t-1} \cdot E^{z,t-1} \left[\frac{mol}{s} \right] \end{aligned} \quad 4.11$$

Number of bubbles conservation

The number of bubbles in a gas compartments (N_b) are calculated by Equation 4.12. By using the number of bubbles and gas holdup, the bubble size is calculated in Equation 4.13.

$$\frac{\partial N_b^z}{\partial t} = \frac{(N_b^{z-1,t} \cdot u_g^{z-1,t-1} - N_b^{z,t-1} \cdot u_g^{z,t-1})}{\Delta z} \quad 4.12$$

$$d_b^{z,t} = \left(\frac{\varepsilon_g^{z,t} \cdot V_{CSTR} \cdot 6}{\pi \cdot N_b^{z,t}} \right)^{1/3} \quad 4.13$$

Equation 4.11 and 4.12 are solved by applying boundary conditions on the discretized balances. The discretization and boundary conditions are explained in Appendix IV.

4.3 Solution strategy

Figure 4.2 depicts the structure of the algorithm solved in MATLAB. The model is solved with a position (z) and time (t) loop. The gas phase is solved for every z -position. The liquid is solved once all gas compartment have been calculated, so that the mass transfer from gas to the liquid can be linked to the liquid phase. The liquid phase of all three compartments (BC1, BC2 and V1) are solved simultaneously with the ode23tb solver from MATLAB. The calculation of gas and liquid continuous from 1 to t_{final} with time step Δt . The time step determines the stability of the solver and is set by the Courant-Friedrichs-Lewy condition, see Equation 4.14.

$$\frac{u_g * \Delta t}{\Delta x} \leq C \quad 4.14$$

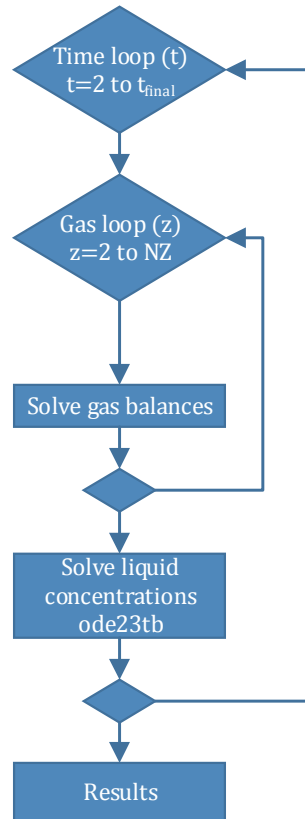


Figure 4.2: Schematic representation of the algorithm to solve the CSTRs in series model for describing the MSBC.

4.4 Bubble cutting implementation

Bubble cutting is implemented in the model by modifying the amount of bubbles present after the wire-mesh ($z=52$) in the column. Equation 4.15 represents the modification in number of bubbles where the cutting constant is larger than one. Due to the cutting and increase of number of bubbles, the bubble diameter decreases. Simultaneously, mass transfer is occurring with these smaller bubble size, therefore, an iteration loop is implemented to conserve mass. The algorithm of solving of gas balances with bubble cutting is schematically displayed in Figure 4.3. Remark that the order of calculation of u_g , ϵ_g and d_b is different when cutting is active. This is due to the fact that the number of bubbles are fixed and the gas holdup is estimated, which results in a defined bubble diameter.

$$N_b^{z,t} = N_b^{z-1,t} * C_{cut} \quad 4.15$$

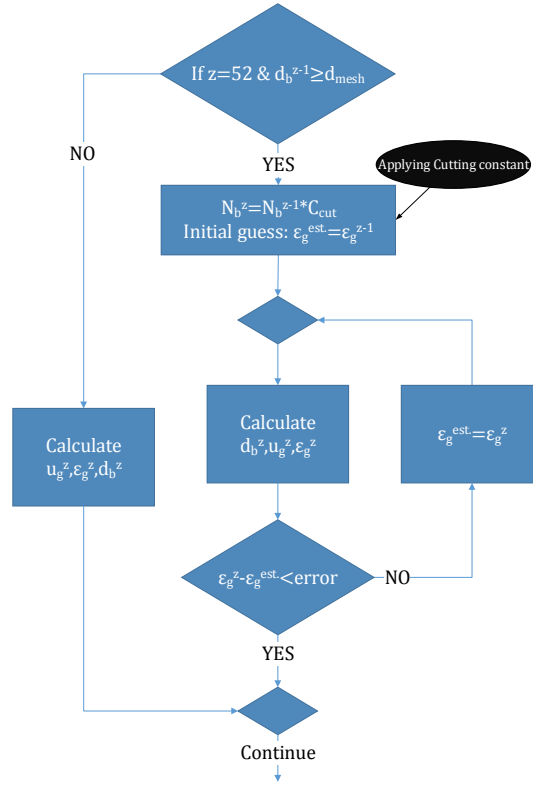


Figure 4.3: Schematic representation of the bubble cutting constant in the gas phase.

4.5 Result sample

An example of the reaction progress in the liquid phase by the concentrations of the four components is displayed in Figure 4.4. The figure shows that at the start of the reaction all absorbed CO_2 reacts to CO_3^{2-} . Just before 50 seconds, the backwards reaction of reaction 2 is becoming dominant, since the concentration of CO_3^{2-} decreases and the concentration of HCO_3^- starts increasing. Until the reaction is over, the HCO_3^- increases and reaches a maximum.

Absorbed CO_2 accumulates, since there is less OH^- to react with and approaches the saturation concentration. Furthermore, a sensitivity analysis on the model is performed and shown in Appendix V.

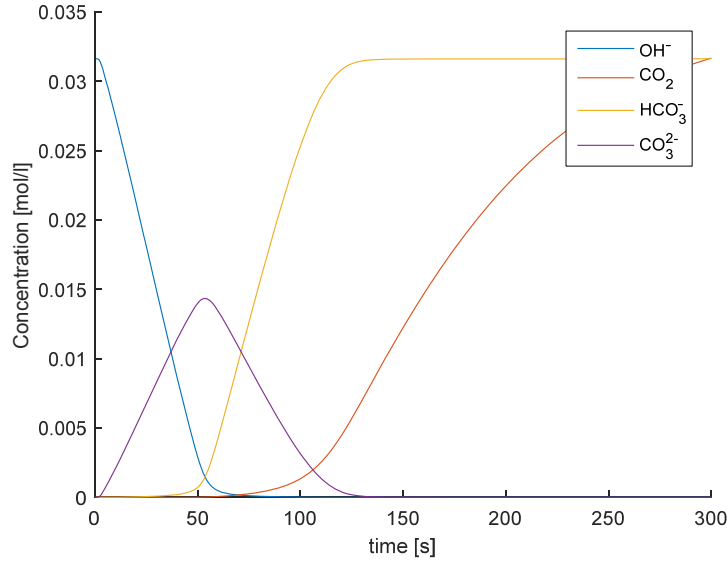


Figure 4.4: Concentration of the four species in the liquid phase over the reaction time. Configuration: No cutting, $u_g=10$ mm/s, $u_l=15$ mm/s.

4.6 Validation parameters

Three different parameters are studied during the experiments to validate the model: bubble size, pH value and gas holdup.

Bubble size

Bubble size is measured using the digital image analysis technique explained in section 2.2. The timing of the image recording is based on predictions of the model. In Figure 4.5, it is shown that the bubble size is becoming constant over the entire column during the reaction (for this configuration around 75 seconds). This must be caused by the constant amount of mass transferred in the column and correspond with a pH of 10.5. Resulting in the first recording point of the bubble size during reaction. The second recording of images is performed when the reaction is over (t_{final}). A recording consist of 1000 images and are taken at a frequency of 50 Hz for all five sections.

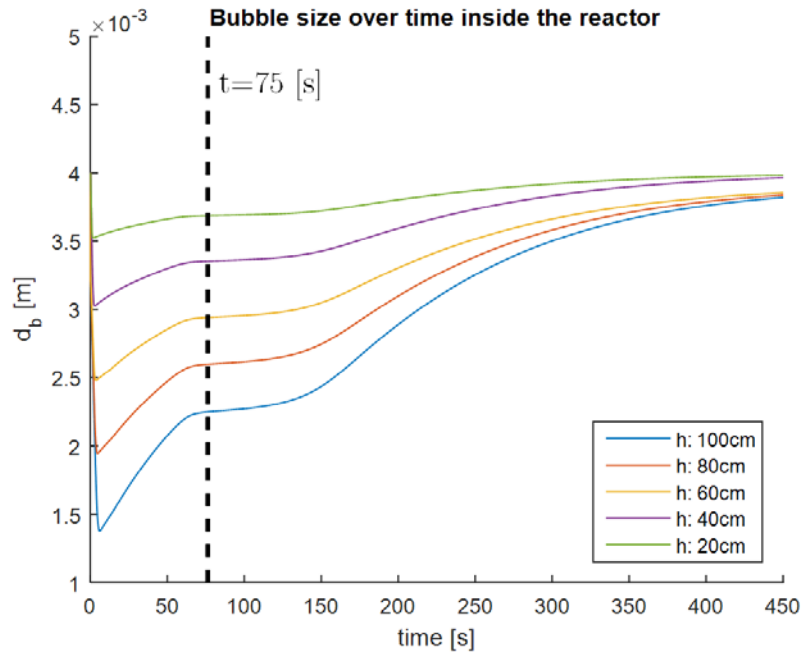


Figure 4.5: Bubble size in the column at different heights in the column derived from the model. Configuration: no cutting, $u_g=10$ mm/s, $u_l=14$ mm/s.

pH value

The pH value in the reactor is compared with the model to track the reaction progress by the presence of hydroxide ion. The pH is measured by using a Metrohm 780 pH-meter which is inserted at the top part of the column, which corresponds to BC2 in the CSTRs in series model. The pH is logged over the entire duration of the reaction and stored on a computer.

Gas holdup

Measuring the gas holdup with the height expansion method (section 2.4) during the reaction is practically unfavourable. When the liquid and gas circulation are stopped simultaneously, the reaction still continues due to the absorbed CO_2 . Therefore, the gas holdup is measured at the end of reaction, to see whether the final gas holdup matches the model.

5 Validation of CSTRs in series model

Validation of the discussed model in Chapter 4 is performed for two configurations, where a wire-mesh with openings of 2.7 mm is used instead of 3.6 mm. This mesh is selected, because the bubble size decreases significantly due to mass transfer (from 4 to 2 mm in size). Therefore, small opening size of a wire-mesh are preferred, since it has a better cutting performance at smaller bubble size. The cutting constant in the model is based on the differences in bubble size before and after the mesh from experiments at the end of the reaction (t_{final}).

Two cases have been studied with an equal amount of liquid (5.5 liter), there configurations are shown in Table 5.1. The first configuration is a case for low gas velocity and intermediate liquid velocity, to validate the model in a homogeneous regime. The second validation is performed with a higher gas flow and a lower liquid velocity. The lower liquid velocity increases the residence time and will increase the influence of the side vessel. The higher gas velocity, changes the homogeneous regime to transition regime. This might cause more coalescence and can result in larger bubble size. This case is used to determine if the model holds in a regime where also bubble coalescence is significantly active.

Table 5.1: Used cutting constant, timings for bubble recording, superficial gas and liquid velocities for the two studied cases to validate the CSTRs in series model.

	<i>Superficial gas velocity [mm/s]</i>	<i>Superficial liquid velocity [mm/s]</i>	C_{cutting}^{**}	$t_{\text{pH}=10.5}$ [s]	t_{final} [s]
Case 1: homogeneous regime	10	14	1.0681	76	600
Case 2: transition regime	15	7	1.0640	50	480

5.1 Case 1: Homogeneous regime

In the model, one uniform bubble size is present in a gas compartment (z), but in experiments a distribution of bubble sizes are present. Therefore, the mean (d_{10}) and Sauter mean (d_{32}) diameter of experiments are shown and compared with the model. Figure 5.1 depicts these results of the bubble size at $t_{\text{pH}=10.5}$ and at t_{final} of the reaction of case 1.

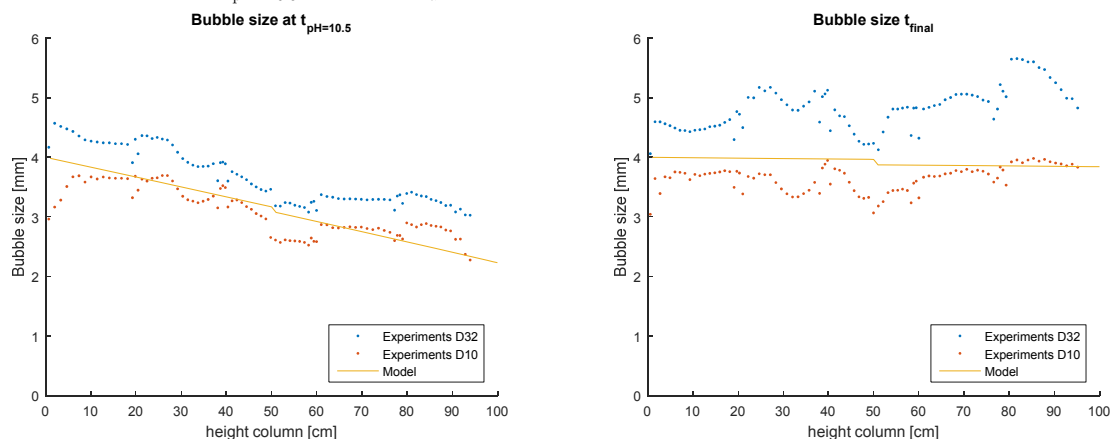


Figure 5.1: Bubble size over the column at two measured times, as explained in section 4.5. Left: during reaction at $\text{pH}=10.5$, right: at the end of reaction. Configuration case 1: wire-mesh 2.7 mm, $u_g=10$ mm/s, $u_l=14$ mm/s.

** Cutting constant based on the difference in bubble size from experiments at t_{final} .

It is observed that the model and experiments have the same trend over the bubble column for both measured times. In both instances the bubble size of the model seem to approximate the experimental data, but higher up the column ($\pm 80\text{cm}$) the model results are slightly lower than the experimental data. This could be due to the activity of coalescence of bubbles. Furthermore, the difference between number mean and Sauter mean diameter is higher at t_{final} . This might be due to the lower mass transfer rate, therefore, larger bubbles ($\pm 4\text{ mm}$) present. These larger bubbles might cause more coalescence, resulting in an even larger bubble size and bigger difference between d_{10} and d_{32} at t_{final} .

Figure 5.2 depicts the pH curve of the model and experiments in BC2 over the reaction time. Firstly, the two inflection points are also seen in the experiments, which means that the kinetics of the model are approaching the experiments well. Overall, the model predicts the experiments very well and also the coupling of the liquid compartments seem to be implemented correctly. The experiments mismatches the model at 150 seconds, when the reaction is almost at its end. At this point, the activity of coalescence might be increased, as was shown by the difference between d_{10} and d_{32} bubble size. Therefore, large bubbles are present, which lead to less mass transfer rates and lead ultimately to a lower decrease in pH value in experiments.

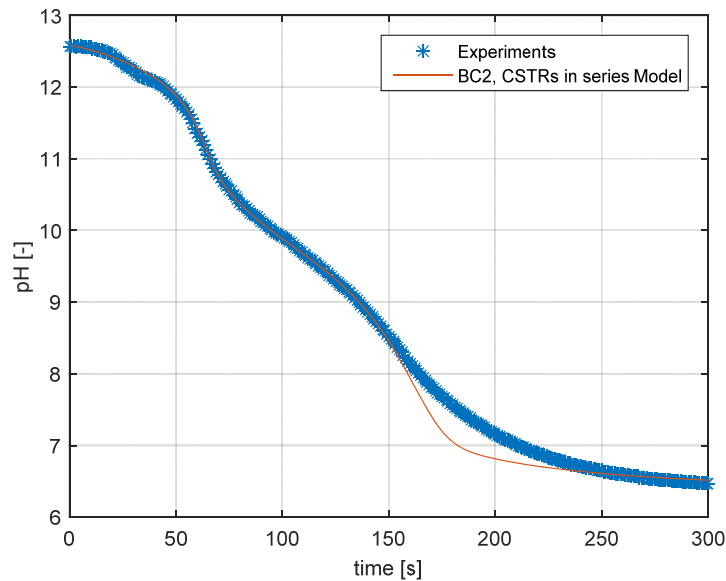


Figure 5.2: Comparison pH curve over time between model and experiments. Configuration case 1: wire-mesh 2.7 mm, $u_g=10\text{ mm/s}$, $w_l=14\text{ mm/s}$.

Figure 5.3 displays the gas holdup of the model compared to the experiments at the end of the reaction. Gas holdup of experiments is 10% higher compared to the model. This could be due to the hydrodynamic resistance caused by the wire-mesh, which is not accounted for in the model. In the experiments bubbles are slowed down by the mesh and will not have the same velocity as in the model. Additionally, axial dispersion could slightly increase the gas holdup of experiments.

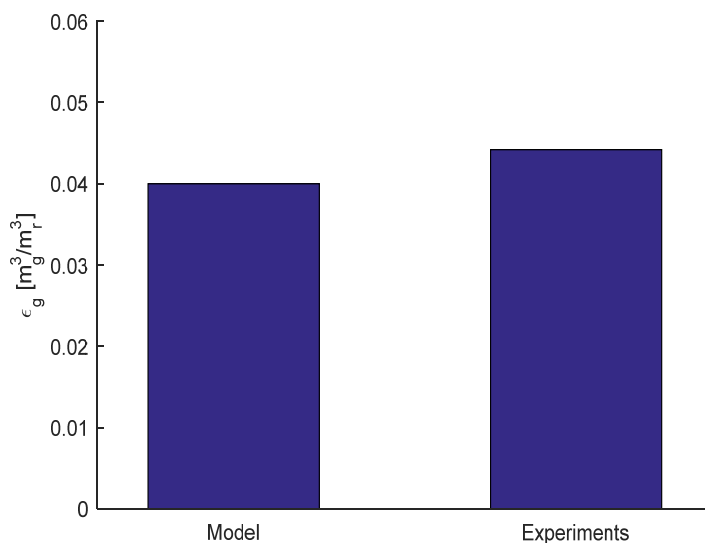


Figure 5.3: Gas holdup comparison between the model and experiments. Configuration case 1: wire-mesh 2.7 mm, $u_g=10$ mm/s, $u_l=14$ mm/s.

5.2 Case 2: Transition regime

The second case is a validation of a higher gas velocity ($u_g=15$ mm/s) and a lower liquid velocity ($u_l=7$ mm/s) by using a wire-mesh with openings of 2.7 mm.

Figure 5.4 depicts the bubble diameter over the column. When looking at the bubble size at $t_{\text{pH}=10.5}$, it is seen that the experiments have a larger bubble size from a column height of approximately 40 cm. As in case 1, this deviation might be caused by bubble coalescence, which is more significant in this transition regime. The bubble size of the model matches better at t_{final} , where the modelling results are between mean and Sauter mean diameter.

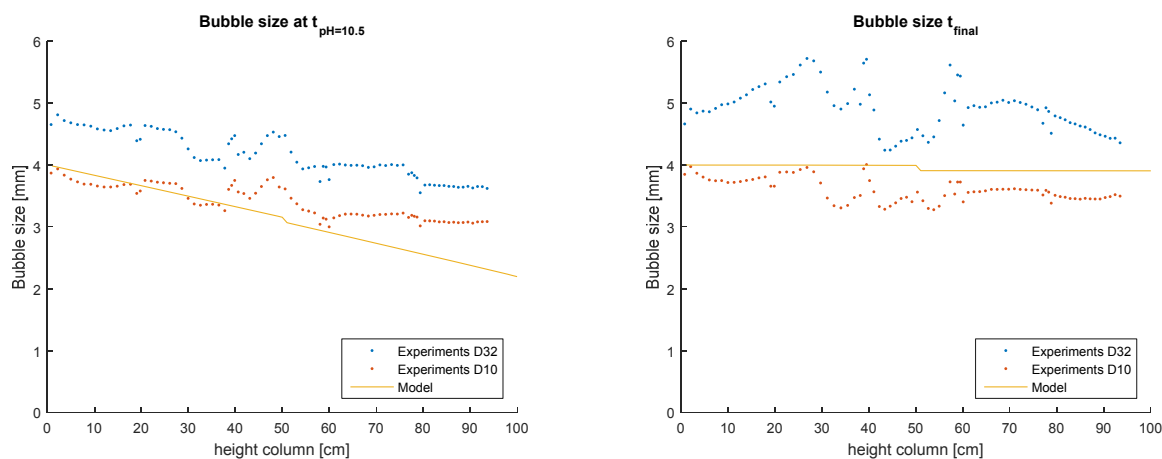


Figure 5.4: Bubble size over the column. Left: during reaction at $\text{pH}=10.5$, right: at the end of reaction. Configuration case 2: wire-mesh 2.7 mm, $u_g=15$ mm/s, $u_l=7$ mm/s.

When an image of case 2 is compared with case 1 at $\text{pH}=10.5$, see Figure 5.5, it is seen that a large diversity of bubble size is present in case 2 and especially larger bubbles are present. This is due to the increasing bubble coalescence with higher gas velocity.

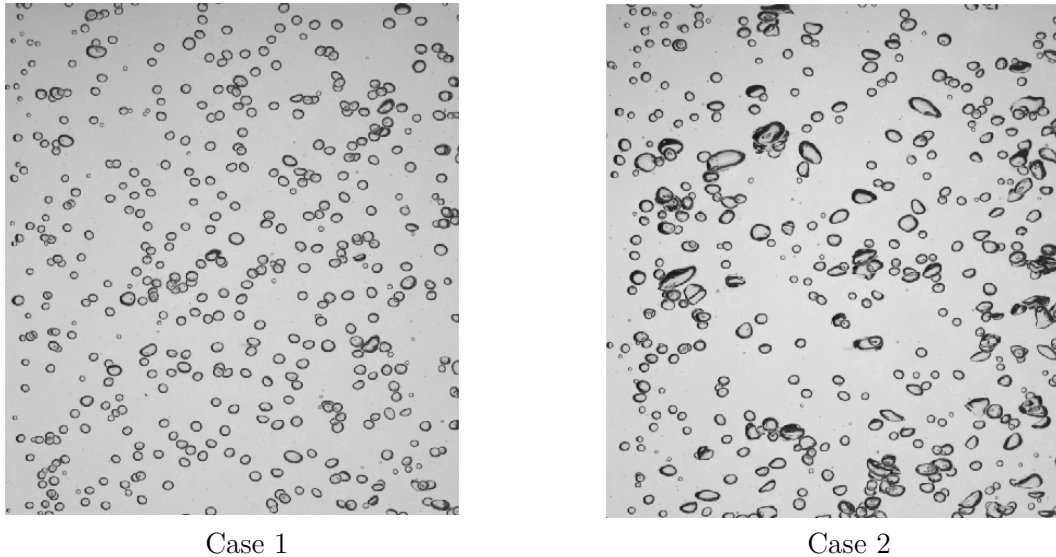


Figure 5.5: Images of the bubbles inside the column at $t=t_{\text{pH}=10.5}$ in section 4 (height from 58 to 79 cm) for case 1 and case 2. Configuration case 1: wire-mesh 2.7 mm, $u_g=10$ mm/s, $w_l=14$ mm/s. Configuration case 2: wire-mesh 2.7 mm, $u_g=15$ mm/s, $w_l=7$ mm/s.

This effect might also explain the deviation in pH value comparison of the experiment with the model of case 2, which is illustrated in Figure 5.6. In the beginning the model matches the experiments well, but at 60-70 seconds the pH of the model is lower than the experiments. The mismatch in the pH-curve from approximately 60 seconds is probably caused by found coalescence of bubbles. This larger bubbles will result in less mass transfer, therefore, the observed reaction in experiments is slower compared to the model.

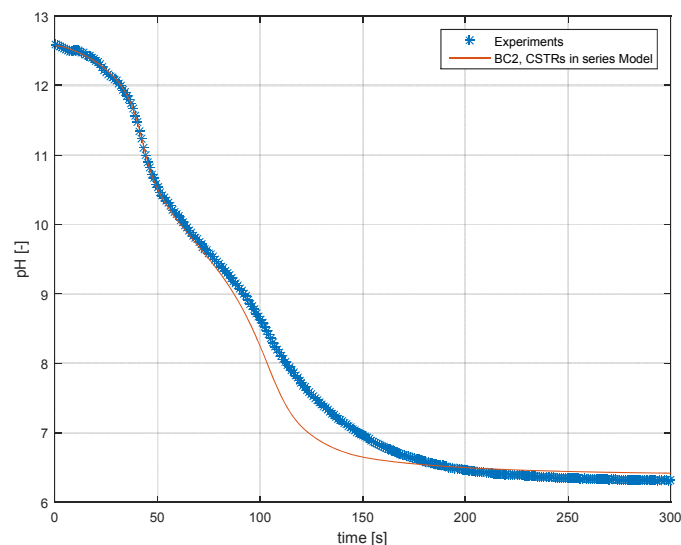


Figure 5.6: Comparison pH curve over time between model and experiments. Configuration case 2: wire-mesh 2.7 mm, $u_g=15$ mm/s, $w_l=7$ mm/s.

Figure 5.7 depicts, the gas holdup of case 2. Similar to case 1, the experiments have a slightly higher gas holdup, which could be caused by the hydrodynamic resistance caused by the wire-mesh, which is not accounted for in the model. Additionally, axial dispersion could slightly increase the gas holdup of experiments.

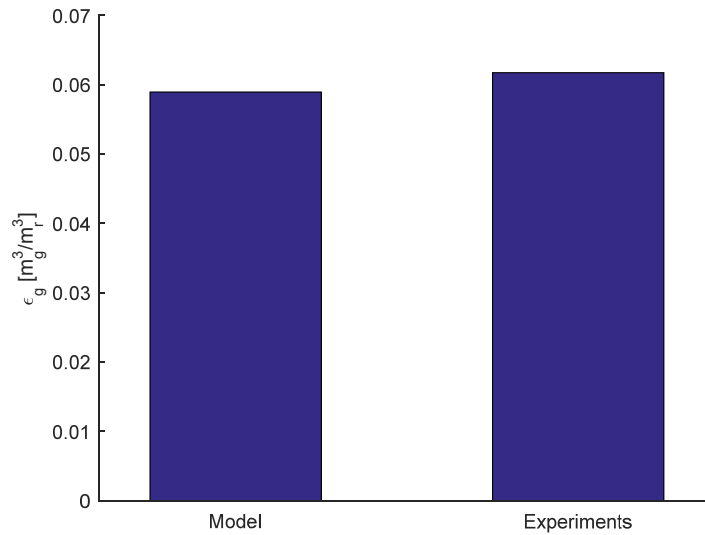


Figure 5.7: Gas holdup comparison model and experiments. Configuration case 2: wire-mesh 2.7 mm, $u_g=15$ mm/s, $u_l=7$ mm/s.

6 Conclusions

Hydrodynamic study

The influence of co-current liquid circulation is investigated in a micro-structured bubble column. The effect of different internals are investigated for various superficial gas and liquid velocities in an air-water system. Digital image analysis (DIA) technique is used to measure the bubble size. The velocity of the bubbles over the column are measured by the particle image velocimetry (PIV) technique. The goal of these internal structures is to decrease the bubble size and increase the specific surface area to enhance mass transfer rates.

Bubble size is found to increase for increasing superficial liquid velocity. Co-current liquid circulation seems to drag the bubbles along with the flow. Furthermore, the largest bubble size is not found at the highest liquid velocity, but at 14 mm/s. Increasing the liquid velocity to 28 mm/s lowered the bubble size, which might be due to the change in break-up and coalescence behaviour.

Bubble velocities inside the column increased when liquid is circulated. At low liquid velocities (7 mm/s), bubble velocity increased to a significant higher bubble velocity. Further increase of liquid velocity (14-28 mm/s) did not result in a significantly higher bubble velocity. The gas holdup results confirm the trends in bubble velocity. The gas holdup decreases significantly at low superficial liquid velocity (7 mm/s). At higher superficial liquid velocities (14-28 mm/s) the decrease in gas holdup is much lower. This result might be due to the lowered drag force which is related to the gas holdup.

Hydrodynamics and cutting behaviour is also studied for different internals and various operating conditions. Increasing liquid velocity did not significantly affect the bubble cutting behaviour of any structured packing. The difference in Sauter mean diameter before and after the packing is similar for all superficial liquid velocities. The most significant bubble cutting is found by using wire-mesh with openings (highest difference in Sauter mean diameter before and after the mesh, Δd_{32}). An important observation is that the Sulzer packing did not enhance bubble cutting significantly. In fact, more big bubbles are seen when Sulzer packing is used. This could be due to the lower bubble velocities before interacting with the Sulzer packing.

Modelling micro-structured bubble column

The micro-structured bubble column is modelled using a CSTRs in series (tanks-in-series) model with bubble cutting included. The liquid phase is simulated as three liquid compartments and the gas phase was simulated as 100 gas compartments, assuming plug flow behaviour. The gas phase did not take into account a distribution of bubble size and coalescence of bubbles are not taken into account. This CSTRs in series model is validated by using two cases: a homogeneous regime (case 1) and a transition regime (case 2).

The first case approached the experiments well and showed that kinetics, gas velocity and liquid compartment linkage was properly implemented. In the second case the influence of bubble

Conclusions

coalescence became more significant, which was observed from the recorded images. This coalescence contribution probably caused the higher deviation in case 2 from the experiments compared to the model.

7 Recommendations

Cutting of bubbles has extensively been investigated within the possibilities of the digital image analysis (DIA) script. At gas holdup higher than 10% this DIA script fails and, therefore, this script might be improved if better filters are available for analysis. Also more advanced techniques like X-ray tomography are optional to improve the bubble detection, which can handle the detection of bubbles at higher gas holdup.

Liquid PIV could be used to track liquid velocities in the column. By using liquid PIV the significance of the moving liquid around the bubbles on the bubble behaviour could be studied in more detail.

If the side vessel of the micro-structured bubble column would be entirely closed, a counter-current operation is possible. This enlarges the gas holdup significantly and is very interesting to study in more detail.

The used pseudo-2D setup in the lab had some leakage. Since this also concerns safety, is essential that the technician checks the entire setup and fixes this problem.

The CSTRs in series model had its limitations due to influence of coalescence. Including a coalescence contribution in the CSTRs in series model might improve the region of application of the model. This could be done by the model proposed by Sommerfeld [20]. Furthermore in this model, swarm effects of bubbles become more active at higher superficial gas velocities and the drag force is influenced by the surrounding bubbles. This swarm effect on the drag coefficient has been described by Roghair [21] and might be useful in further development of the model.

Acknowledgements

After a 9 months graduation project within the SMR group, I would like to share some words for the people who helped me during the project.

First of all, I would like to thank professor Kuipers for giving me the opportunity to graduate within the multiphase reactors (SMR) group. Additionally, I would like to thank professor Deen for his effort in my project. Although he moved from associate professor within the SMR group to full professor in Multiphase & Reactive Flows group of Mechanical engineering he wanted to help me finish the job I had started. Furthermore, I would like to thank professor Meuldijk for his willingness to participate in the graduation committee, although he retired since the 1th May 2016.

Next, I would like to thank the entire SMR group, who were always interested in what I was doing and willing to provide their input during the project. Then, I would like to thank the technicians (Thijs, Joris and Joost) for helping me during this project with my setup and for their input about the practical problems. Also I would like to thank Peter Lipman for helping me with the conductivity meter for the tracer experiments.

Furthermore, I would like to thank my family and friends for listening to me about my project and help me wherever they could to make this project a success.

Finally, I would like to thank my mentor Krushnathej Sujatha Thiruvalluvan. He has provided me a lot of guidance, support and motivation during the project. I really liked the structure and the regular meetings to discuss the progress and the criticism over the results. I would like to wish him all the best for the final months as a PhD-student here at the TU/e

Bibliography

- [1] Darmana D., Henket R.L.B., Deen N.G., Kuipers J.A.M., “Detailed modelling of hydrodynamics, mass transfer and chemical reactions in a bubble column using discrete bubble model: Chemisorption of CO₂ into a NaOH solution, numerical and experimental study,” *Chem. Eng. Sci.*, vol. 62, no. 9, pp. 2556-2575, 2007.
- [2] Sujatha K.T., Meeusen B.G.J., Kuipers J.A.M., and Deen N.G., “Experimental studies of bubbly flow in a pseudo-2D micro-structured bubble column reactor using digital image analysis,” *Chem. Eng. Sci.*, vol. 130, pp. 18-30, 2015.
- [3] Biń A.K., Duczmal B., Machniewski P., “Hydrodynamics and ozone mass transfer in a tall bubble column,” *Chem. Eng. Sci.*, vol. 56, no. 21-22, pp. 6233-6240, 2001.
- [4] Pjontek D., Parisien V., Macchi A., “Bubble characteristics measured using a monofibre optical probe in a bubble column and freeboard region under high gas holdup conditions,” *Chem. Eng. Sci.*, vol. 111, pp. 153-169, 2014.
- [5] Jin H., Yang S., He G., Wang M., Willimans R.A., “The effect of gas-liquid counter-current operation on gas hold-up in bubble columns using electrical resistance tomography,” *J Chem Technol Biotechnol*, vol. 85, pp. 1278-1283, 2010.
- [6] Meeusen B.G.J., “Mass transfer in bubble columns with wire mesh,” Eindhoven University of Technology, Eindhoven, 2014.
- [7] Höller V., Wegracht W., Kiwi-Minsker L., Renken A. , “Fibrous structured catalytic beds for three-phase reaction engineering: Hydrodynamics study in staged bubble columns,” *Catalysis Today*, vol. 60, pp. 51-56, 2000.
- [8] Rabha S., Schubert M., Grugel F., Banowski M., Hampel U., “Visualization and quantitative analysis of dispersive mixing by helical static mixer in upwards co-current gas-liquid flow,” *Chemical Engineering Journal*, vol. 262, pp. 527-540, 2015.
- [9] Deen N.G., Mudde R.F., Kuipers J.A.M., Zehner P., Kraume M., “Bubble columns,” in *Ulman's Encyclopedia of Industrial Chemistry*, Wiley-VCH, 2012, pp. 359-279.
- [10] Höller V., Wegracht D., Kiwi-Minsker L., Renken A., “Fibrous structured catalytic beds for three-phase reaction engineering hydrodynamics study in staged bubble columns.,” *Catalysis Today*, vol. 60, pp. 51-56, 2000.
- [11] Chen B.H., Yang N.S., “Characteristics of a Cocurrent Multistage Bubble Column,” *Ind. Eng. Chem.*, vol. 28, pp. 1405-1410, 1989.
- [12] M. Asgharpour M. Reza Mehrnia N Mostoufi, “Effect of surface contaminants on oxygen transfer in bubble column reactors,” *Biochemical Engineering Journal*, vol. 49, pp. 351-360, 2010.
- [13] Kamath S., “Micro-structured Bubble Column: An Experimental and Numerical Study,” Technical University Eindhoven, Eindhoven, 2015.
- [14] Lau Y. M., Coalescence & break-up in dense bubbly flows, Eindhoven: Eindhoven University of Technology, 2013.

- [15] Pohorecki R., Moniuk W., “Kinetics of reaction between carbon dioxide and hydroxyl ions in aqueous electrolyte solutions,” *Chemical Engineering Science*, vol. 43, pp. 1677-1684, 1988.
- [16] Bhat R.D., Kuiper J.A.M., Versteeg G.F., “Mass transfer with complex chemical reactions in gas-liquid systems: two-step reversible reactions with unit stoichiometric and kinetic orders,” *Chemical Engineering Journal* 76, vol. 76, pp. 127-152, 2000.
- [17] Hikita H. Asai S. Takatsuka T., “Absorption of Carbon Dioxide into Aqueous Sodium Hydroxide and Sodium Carbonate-Bicarbonate Solutions,” *The Chemical Engineering Journal*, vol. 11, pp. 131-141, 1976.
- [18] M. Vladimir, “Bubble Column Design of CO₂ chemisorption into NaOH solution,” Stan Ackermans Institute, Eindhoven, 2013.
- [19] Tomiyama A., Kataoka I., Zun I., Sakaguchi T., “Drag coefficients of single bubbles under normal and micro gravity conditions,” *JSME international journal*, vol. 41, no. 2, pp. 471-479, 1998.
- [20] Sommerfeld M., Bourloutski E., Bröder D., “Euler / Lagrange Calculations of Bubbly Flows with Consideration of Bubble Coalescence,” *Canadian Journal Of Chemical Engineering*, vol. 81, pp. 508-518, 2003.
- [21] Lau Y.M., Roghair I., Deen N.G., van Sint Annaland M., Kuipers J. A. M., “Numerical investigation of the drag closure for bubbles in bubble swarms,” *Chemical Engineering Science*, vol. 66, pp. 3309-3316, 2011.
- [22] Q. Wu X. Wang T. Wang M. Han Z. Sha J. Wang , “Effect of liquid viscosity on hydrodynamics and bubble behaviour of an external-loop airlift reactor,” *The Canadian Journal of Chemical Engineering*, vol. 91, no. 12, pp. 1957-1963, 2013.
- [23] H. Li and A. Prakash, “Heat Transfer and Hydrodynamics in a Three-Phase Slurry Bubble Column,” *Ind. Eng. Chem. Res.*, vol. 36, pp. 4688-4694, 1997.
- [24] Shah Y.T., Kelkar B.G., Godbole S.P., Deckwer W. D., “Design parameters estimation for bubble column reactors,” *AIChE Journal*, vol. 28, no. 3, pp. 353-379, 1982.
- [25] M. Barigou M. Greaves, “A capillary suction probe for bubble size measurement,” *Meas. Sci. Technol.* 2, pp. 318-326, 1991.
- [26] Thiruvalluvan Sujatha, K., CO₂ Chemical Absorption into NaOH(aq) solutions in dense bubbly flow, Eindhoven: Technical University Eindhoven, 2012.

Appendix I: Visual observation results.

This appendix shows the results of the visual observation. Table I.1 is the legend, and the results are shown in Table I.2 to I.6.

Table I.1: Legend visual observation results.





Colour	Cutting behaviour
	Bubbles flow nicely through mesh, some cutting
	Big bubbles flow through wire-mesh but mostly re-coalesce after mesh, cutting occurs
	Most bubbles flow through mesh, small gas-cushion on the sides, cutting occurs
	Formation of gas-cushion bubbles accumulate, almost no cutting

Table I.2: Results visual observation, $u_l = 0$ mm/s.































$u_l=0$ [mm/s]		u_g [mm/s]					
		5	10	15	20	25	30
Wire-mesh/ Packing	Sulzer						
	3,6						
	3,3						
	2,7						
	2,2						

Table I.3: Results visual observation, $u_l = 7$ mm/s.































$u_l=7$ [mm/s]		u_g [mm/s]					
		5	10	15	20	25	30
Wire-mesh/ Packing	Sulzer						
	3,6						
	3,3						
	2,7						
	2,2						

Table I.4: Results visual observation, $u_l = 14$ mm/s.































$u_l=14$ [mm/s]		u_g [mm/s]					
		5	10	15	20	25	30
Wire-mesh/ Packing	Sulzer						
	3,6						
	3,3						
	2,7						
	2,2						

Table I.5: Results visual observation, $u_l = 21$ mm/s.

$u_l = 21$ [mm/s]		u_g [mm/s]					
		5	10	15	20	25	30
Wire-mesh/ Packing	Sulzer	Blue	Blue	Green	Green	Green	Green
	3,6	Blue	Blue	Green	Green	Green	Green
	3,3	Blue	Blue	Green	Green	Green	Green
	2,7	Blue	Blue	Green	Green	Green	Green
	2,2	Red	Red	Yellow	Green	Green	Green

Table I.6: Results visual observation, $u_l = 28$ mm/s.

$u_l = 28$ [mm/s]		u_g [mm/s]					
		5	10	15	20	25	30
Wire-mesh/ Packing	Sulzer	Blue	Blue	Green	Green	Green	Green
	3,6	Blue	Blue	Green	Green	Green	Green
	3,3	Blue	Blue	Green	Green	Green	Green
	2,7	Blue	Blue	Blue	Green	Green	Green
	2,2	Red	Red	Yellow	Green	Green	Green

Appendix II: Bubble size and VPD at low superficial gas velocities.

At lower superficial gas velocity, the same results are found as gas velocity set to 20 mm/s. Two different probability densities are examined with small bubbles included (<1.2 mm). The PDF shows that the first peak has the following order of peak height: [0; 7; 28 and 14 mm/s]. The second peak has the exactly opposite order. The VPD corresponds nicely to the PDF and it shows that in the same order the VPD gets a more Gaussian behaviour. This results in a higher average bubble size. Especially at high bubble sizes (8-12 mm), the increase of velocity lowers the amount of big bubbles. On the other hand, less small bubbles are present (<2 mm) with increase of superficial liquid velocity. These results correspond to the findings of a superficial gas velocity of 20 mm/s.

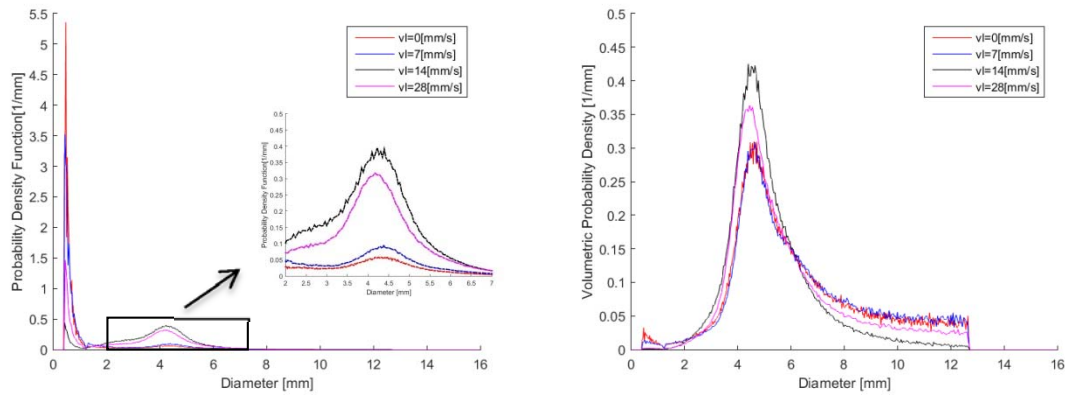


Figure II.1: Probability density function and volumetric probability density function. Configuration: no mesh, $u_g=10$ mm/s.

Appendix III: Sherwood correlations

Different configurations for the Sherwood correlation has been found. In this appendix some of these correlations are discussed and there application field is described. The basic form of the Sherwood correlation is:

$$Sh = \frac{k_l^j d_b}{D^j} = 2.0 + aRe^b Sc^c \quad \text{III.1}$$

Henket used two sets of constants. The coefficients of set A are: a=1.25, b=0.5 and c=1/3. The second set of constants (B) are: a=0.43, b=0.58 and c=1/3. Brauer and Mewes proposed a correlation for ellipsoid bubbles, taking into account the influence of deformation turbulence is given by III.2. Hughmark proposed a correlation which takes swarms of bubbles into account shown in Equation III.3. Bird proposed a Sherwood correlation in the case of mass transfer for flows around spheres, showed by Equation III.4.

$$Sh = 2 + 0.015Re^{0.89} Sc^{0.7} \quad \text{III.2}$$

$$Sh = 2 + 0.0187Re^{0.779} Sc^{0.546} \left(\frac{d_b g^{1/3}}{D^{2/3}} \right)^{0.116} \quad \text{III.3}$$

$$Sh = 2 + 0.6415(ReSc)^{1/2} \quad \text{III.4}$$

Figure III.1 depicts the result of CO₂ absorption using these five correlations to give an overview. It is seen that Brauer and Meyer predicts the highest CO₂ absorption and the B correlation of Henket the lowest.

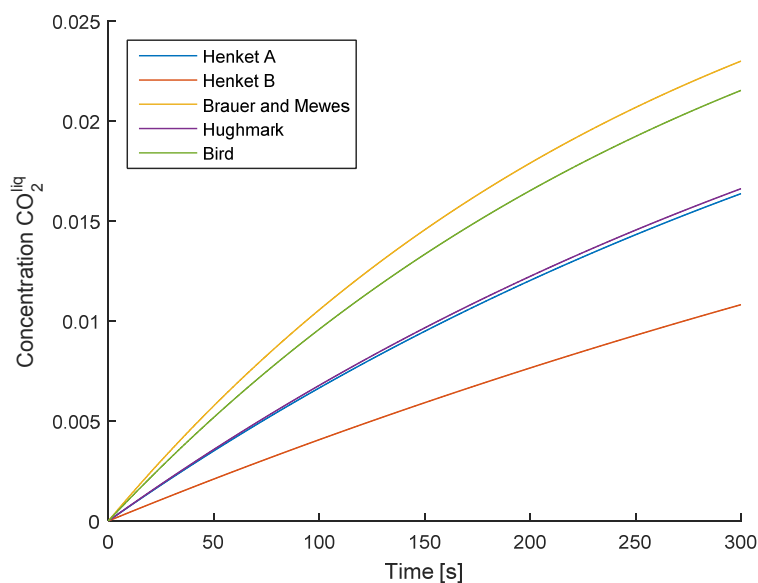


Figure III.1: Comparison of different Sherwood correlations to predict mass transfer of absorption of CO₂ in NaOH.

Appendix IV: Discretization and boundary conditions

Discretization

Discretization of the mass conservation Equation 4.11 and rewriting it yields the gas holdup equation solved in the CSTRs in series model.

$$\begin{aligned} \frac{\partial(CO_2^g \cdot \varepsilon_g^z \cdot V_{CSTR})}{\partial t} &= A_{BC} \cdot CO_2^g \cdot (\varepsilon_g^{z-1,t} \cdot u_g^{z-1,t} - \varepsilon_g^{z,t} \cdot u_g^{z,t}) - (H_{BC1/BC2} \cdot CO_2^g \\ &- [CO_2]_{BC1/BC2}^{t-1}) \cdot N_b^{z,t-1} \cdot k_l^{z,t-1} \cdot A_b^{z,t-1} \cdot E^{z,t-1} \left[\frac{mol}{s} \right] \end{aligned} \quad 4.11$$

$$\begin{aligned} \frac{\partial(\varepsilon_g^z \cdot V_{CSTR})}{\partial t} &= A_{BC} \cdot (\varepsilon_g^{z-1,t} \cdot u_g^{z-1,t} - \varepsilon_g^{z,t} \cdot u_g^{z,t}) - \left(H_{BC1/BC2} - \frac{[CO_2]_{BC1/BC2}^{t-1}}{CO_2^g} \right) \cdot N_b^{z,t-1} \cdot k_l^{z,t-1} \\ &\cdot A_b^{z,t-1} \cdot E^{z,t-1} \end{aligned}$$

$$\begin{aligned} \frac{\partial(\varepsilon_g^z)}{\partial t} &= \frac{1}{\Delta z} \cdot (\varepsilon_g^{z-1,t} \cdot u_g^{z-1,t} - \varepsilon_g^{z,t} \cdot u_g^{z,t}) - \frac{1}{V_{CSTR}} \cdot \left(H_{BC1/BC2} - \frac{[CO_2]_{BC1/BC2}^{t-1}}{CO_2^g} \right) \cdot N_b^{z,t-1} \\ &\cdot k_l^{z,t-1} \cdot A_b^{z,t-1} \cdot E^{z,t-1} \end{aligned}$$

Discretisation of Equation of the above Equation yields:

$$\varepsilon_g^{z,t} = \frac{\left(\varepsilon_g^{z,t-1} + \frac{\Delta t}{\Delta z} \cdot (\varepsilon_g^{z-1,t} \cdot u_g^{z-1,t}) - \frac{\Delta t}{V_{CSTR}} \cdot N_b^{z,t-1} \cdot k_l^{z,t-1} \cdot A_b^{z,t-1} \cdot E^{z,t-1} \cdot \left(H_{BC1/BC2} - \frac{[CO_2]_{BC1/BC2}^{t-1}}{CO_2^g} \right) \right)}{1 + \frac{\Delta t \cdot u_g^{z,t}}{\Delta z}}$$

The balance of the number of bubbles (4.12) is discretize to

$$\begin{aligned} \frac{\partial N_b^z}{\partial t} &= \frac{(N_b^{z-1,t} \cdot u_g^{z-1,t} - N_b^{z,t} \cdot u_g^{z,t})}{\Delta z} \quad 4.12 \\ N_b^{z,t} &= \frac{N_b^{z,t-1} + \frac{\Delta t}{\Delta z} \cdot N_b^{z-1,t} \cdot u_g^{z-1,t}}{1 + \frac{\Delta t}{\Delta z} \cdot u_g^{z,t}} \end{aligned}$$

Boundary conditions

The corresponding boundary conditions of the gas phase of ε_g (4.11) and N_b (4.12)

Initial conditions gas phase

$$\begin{aligned} t=1 \quad z > 1 \quad \varepsilon_g &= 0 \\ t=1 \quad z > 1 \quad N_b^{z,t} &= 0 \end{aligned}$$

Boundary conditions

$$\begin{aligned} t=\text{all} \quad z=1 \quad \varepsilon_g &= 1 \\ t=\text{all} \quad z=1 \quad N_b^{z,t} &= \frac{\varepsilon_g \cdot V_{CSTR}}{\pi^* (d_b^{z,t})^3} \text{ with } \varepsilon_g=1 \text{ and } d_b=4e^{-3} \end{aligned}$$

Initial conditions liquid phase

t=0	$[\text{OH}^-]^{\text{all}}$	0.0316 [mol/l] (pH=12.5)
t=0	$[\text{CO}_2]^{\text{all}}$	0 [mol/l]
t=0	$[\text{HCO}_3^-]^{\text{all}}$	0 [mol/l]
t=0	$[\text{CO}_3^{2-}]^{\text{all}}$	0 [mol/l]
t=0	u_1	u_1^{sup}

Appendix V: Sensitivity analysis CSTRs in series model

The influence of multiple parameters on the outcomes of the CSTRs in series model are displayed in this appendix. The studied parameters are displayed in Table V.1. All figures are produced by changing specific parameter to the comparing value, so only this value differs from the base case.

Table V.1: Studied parameters for the sensitivity analysis.

Parameter	Base case	Comparing value	Figure
Superficial gas velocity	10 [mm/s]	25 [mm/s]	a
Superficial liquid velocity	15 [mm/s]	5 [mm/s]	b
Number of liquid compartments to simulate the bubble column behaviour	2 [-]	1 [-]	c
Volume of the side vessel	1 [liter]	2 [liter]	d

Figure V.1 displays the pH graphs of the base case for all simulated compartments. Compartment BC1 reacts has the largest decrease in the beginning of all three compartments. However, further in the reaction, the pH of BC2 is lower due to the instream of the liquid from V1 with a higher pH. Furthermore, the side vessel has a significant deviation from the bubble column compartments.

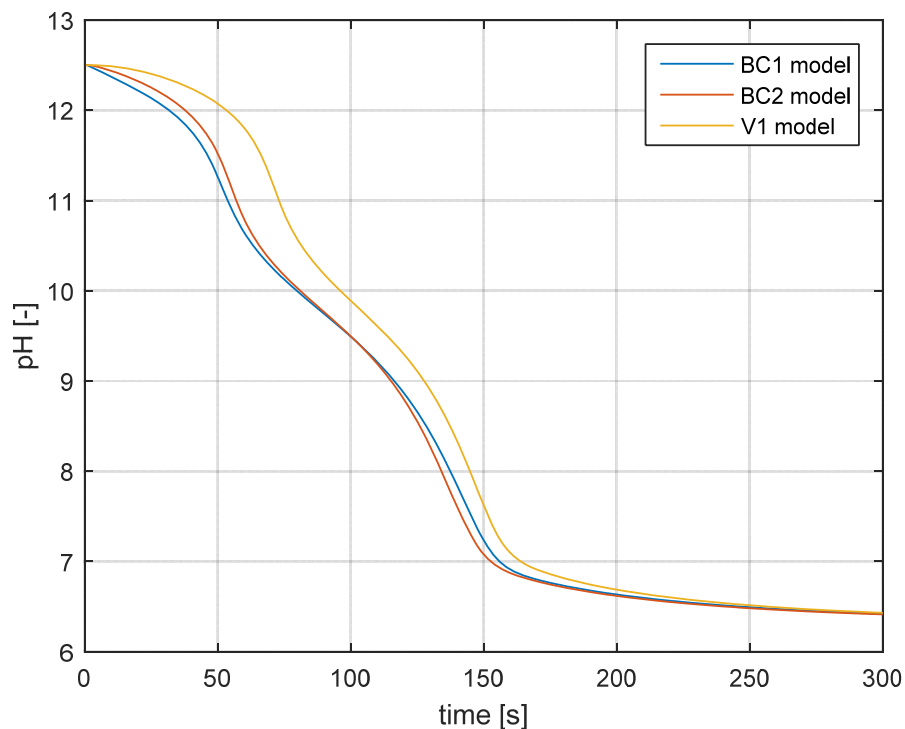


Figure V.1: pH curves of BC1, BC2 and V1 for the base case, corresponding to Table V.1.

Figure V.2 displays the pH curves of the six different configurations of Table V.1. Figure V.2a shows that increasing gas velocity reduces the time of reaction. Decreasing liquid velocity (Figure V.2b) influences the side vessel and the first compartment of the bubble column significantly. Figure V.2c shows the graphs of the simulation of the bubble column as one CSTR. These graph is similar compared to the base case for this configuration. Figure V.2d depicts that enlarging the side vessel, influences BC1 and V1 significantly.

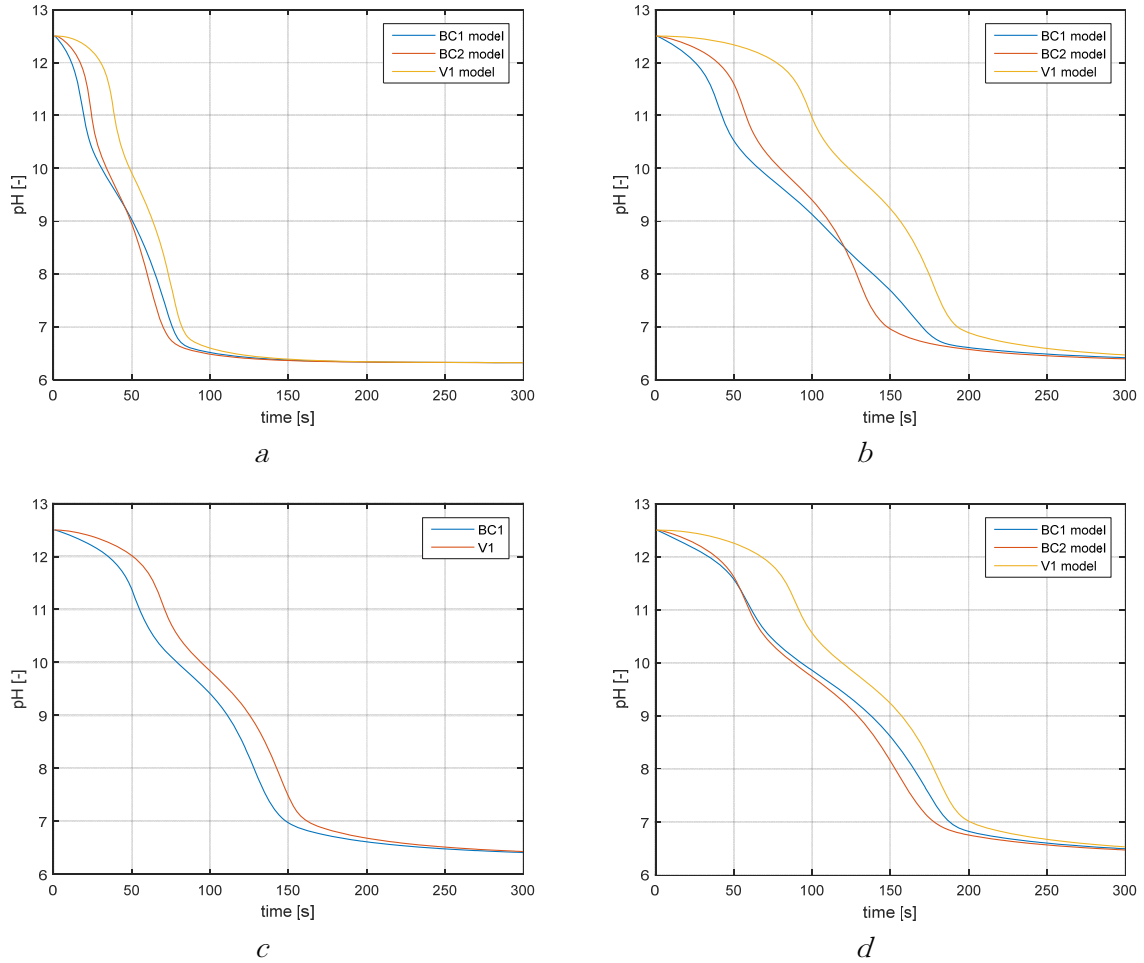


Figure V.2: pH curves of all compartments for the six evaluated parameters corresponding to Table V.1. a) Increase gas velocity from 10 to 25 mm/s, b) decrease liquid velocity from 15 to 5 mm/s, c) amount of liquid compartments is reduced from 2 to 1 and d) volume of the side vessel is increased from 1 to 2 liter.